AGU PUBLICATIONS

JGR

Journal of Geophysical Research: Oceans

RESEARCH ARTICLE

10.1002/2014JC010450

Infragravity-wave dynamics in a barred coastal region, a numerical study

Dirk P. Rijnsdorp[1], Gerben Ruessink[2], and Marcel Zijlema[1]

[1]Environmental Fluid Mechanics Section, Faculty of Civil Engineering and Geosciences, Delft University of Technology, Delft, Netherlands, [2]Department of Physical Geography, Faculty of Geosciences, Utrecht University, Utrecht, Netherlands

Key Points:
- Nearshore infragravity waves are examined using a nonhydrostatic wave model
- Infragravity losses are large near the shore, due breaking and bottom friction
- Bar-trapped edge waves are generally energetic at the outer bar

Correspondence to:
D. P. Rijnsdorp,
D.P.Rijnsdorp@tudelft.nl

Citation:
Rijnsdorp, D. P., G. Ruessink, and M. Zijlema (2015), Infragravity-wave dynamics in a barred coastal region, a numerical study, *J. Geophys. Res. Oceans*, *120*, doi:10.1002/2014JC010450.

Received 16 SEP 2014
Accepted 7 MAY 2015
Accepted article online 12 MAY 2015

Abstract This paper presents a comprehensive numerical study into the infragravity-wave dynamics at a field site, characterized by a gently sloping barred beach. The nonhydrostatic wave-flow model SWASH was used to simulate the local wavefield for a range of wave conditions (including mild and storm conditions). The extensive spatial coverage of the model allowed us to analyze the infragravity-wave dynamics at spatial scales not often covered before. Overall, the model predicted a wavefield that was representative of the natural conditions, supporting the model application to analyze the wave dynamics. The infragravity-wave field was typically dominated by leaky waves, except near the outer bar where bar-trapped edge waves were observed. Relative contributions of bar-trapped waves peaked during mild conditions, when they explained up to 50% of the infragravity variance. Near the outer bar, the infragravity-wave growth was partly explained by nonlinear energy transfers from short waves. This growth was strongest for mild conditions, and decreased for more energetic conditions when short waves were breaking at the outer bar. Further shoreward, infragravity waves lost most of their energy, due to a combination of nonlinear transfers, bottom friction, and infragravity-wave breaking. Nonlinear transfers were only effective near the inner bar, whereas near the shoreline (where losses were strongest) the dissipation was caused by the combined effect of bottom friction and breaking. This study demonstrated the model's potential to study wave dynamics at field scales not easily covered by in situ observations.

1. Introduction

In coastal regions, the wavefield is a composite of short waves, with periods ranging 2–20 s, and infragravity waves, with periods ranging 20–200 s [e.g., *Munk*, 1949; *Tucker*, 1950]. Infragravity waves have small heights (<1 cm) in deep water [e.g., *Webb et al.*, 1991], but their magnitude increases with decreasing water depth. Close to the shore, their height can increase to the order of 1 m, especially during storm conditions [e.g., *Guza and Thornton*, 1982]. Numerous studies have shown the relevance of infragravity waves in nearshore regions. For example, infragravity waves are important in the process of beach [e.g., *Russell*, 1993] and dune erosion [e.g., *van Thiel de Vries et al.*, 2008], may cause harbor resonance [e.g., *Bowers*, 1977], and can have a significant impact on moored ships [e.g., *Naciri et al.*, 2004; *van der Molen et al.*, 2006].

The dynamics of infragravity waves have been extensively investigated by means of theoretical, field, laboratory, and numerical studies. Theoretical studies have shown that infragravity waves are generated by nonlinear interactions between pairs of short waves [e.g., *Longuet-Higgins and Stewart*, 1960; *Hasselmann*, 1962; *Symonds et al.*, 1982]. When shoreward-propagating infragravity waves do not fully dissipate, infragravity waves reflect at the shoreline, which results in a standing infragravity-wave pattern in the nearshore [e.g., *Guza and Thornton*, 1985]. Recent studies have shown that infragravity waves can dissipate a significant amount of their energy close to the shore [e.g., *van Dongeren et al.*, 2007; *Pomeroy et al.*, 2012; *de Bakker et al.*, 2014]. Three mechanisms have been proposed in the literature that can cause energy losses at the infragravity frequencies. First, studies have indicated that energy can be transferred from the infragravity waves to the short waves [*Thomson et al.*, 2006; *Henderson et al.*, 2006; *Ruju et al.*, 2012; *Guedes et al.*, 2013]. Second, infragravity waves can break and lose most of their energy in a region close to the shore [*van Dongeren et al.*, 2007; *de Bakker et al.*, 2014, 2015]. Third, infragravity waves can lose energy due to bottom friction, although this mechanism is mainly significant in the case of extensive shallow regions such as coral reefs [*Pomeroy et al.*, 2012; *Van Dongeren et al.*, 2013].

© 2015. American Geophysical Union. All Rights Reserved.

Seaward directed infragravity waves can propagate to deep water (i.e., leaky waves) or can be trapped in the nearshore by refraction (i.e., edge waves). Several field studies have indicated that most seaward directed infragravity waves are trapped nearshore [e.g., *Okihiro et al*., 1992; *Herbers et al*., 1995]. At beaches with relative monotonic depth variations, field observations of edge waves were in agreement with analytical solutions of edge waves on a plane beach [e.g., *Oltman-Shay and Guza*, 1987; *Huntley et al*., 1981]. These edge-wave solutions are characterized by a maximum amplitude at the shoreline, and an exponential decay in seaward direction. However, edge-wave solutions are significantly altered on beaches with bars [*Kirby et al*., 1981; *Schönfeldt*, 1994; *Bryan and Bowen*, 1996; *Bryan et al*., 1998], and in the presence of strong longshore currents [*Kenyon*, 1972; *Howd et al*., 1992; *Bryan and Bowen*, 1998]. In the case of a barred beach, edge waves can be trapped at the location of a bar. Such bar-trapped edge waves have a cross-shore structure that is characterized by a maximum amplitude near the crest of the bar, and an exponential decay away from this location. *Bryan et al*. [1998] found that bar-trapped edge waves dominated the edge-wave motion near the bar. Strong longshore currents can have a similar effect on the edge-wave solution, and their effect is analogous to a modification of the actual bottom profile [*Howd et al*., 1992; *Bryan and Bowen*, 1998]. However, in the case of a pronounced bar, *Bryan and Bowen* [1998] found that the effect of the longshore current was generally not strong enough to significantly alter edge-wave trapping.

Numerous observational studies have been conducted at natural beaches using relatively short and sparse—but expensive—alongshore arrays of current and/or pressure sensors, combined with sophisticated estimation techniques to facilitate an analyses at infragravity-wave scales [e.g., *Oltman-Shay and Guza*, 1987]. Although laboratory studies are easier instrumented, the scales over which infragravity waves occur, and their sensitivity to bathymetric features and alongshore currents complicates a realistic replication of their nearshore dynamics in a laboratory setting. As an alternative, we use a wave resolving model to study the complex nearshore infragravity-wave evolution that occurs in a natural environment. The extensive spatial coverage of the model output supplemented spatially sparse in situ observations, allowing us to study the variability of the infragravity-wave dynamics on a scale that was not often covered before. Amongst others, this allowed us to differentiate between the contribution of trapping and dissipation to the nearshore infragravity energy balance.

In this study, we used the recently developed SWASH model (Simulating WAves till SHore) [*Zijlema et al*., 2011] to simulate a range of wave conditions that were measured at a field site near Egmond aan Zee (Netherlands) as part of the Coast3D field campaign [e.g., *Ruessink et al*., 2001]. The simulated wave conditions were varied from relatively mild to severe conditions, to gain insight in the spatial variability of the infragravity-wave dynamics for various wave conditions. Section 2 presents a description of the experimental data set, followed by a description of the numerical model. As a prerequisite to analyze the wave dynamics based on the model results, section 3 compares predicted and observed wave parameters (e.g., wave heights), to assess if the predicted wavefield represented the observed wave conditions. Section 4 presents a comprehensive analysis of the infragravity-wave dynamics. This includes an analysis of the spatial structure of the infragravity-wave field (e.g., identifying the presence of leaky and edge waves); and an analysis of the nearshore infragravity energy balance, to quantify energy exchanges between the short and infragravity waves, and to determine which dissipation mechanisms were significant. The results of this study are discussed in section 5 and summarized in section 6.

2. Methodology

2.1. Field Experiment

Measurements of the wavefield were obtained from October to November 1998 at a sandy beach near Egmond aan Zee, Netherlands [*Ruessink et al*., 2001]. Four bidirectional current meters and 10 pressure sensors were positioned at the experimental site, which is characterized by a double bar system and a gentle slope (see Figure 1). The instruments acquired data for approximately 34 min every hour, at a sampling rate of 2 or 4 Hz. A directional wave rider buoy, located 5 km offshore at a depth of 16 m, measured offshore wave conditions (the significant wave height $H_{m_0,d}$, peak period $T_{p,d}$, and energy-weighted mean direction $\bar{\theta}_d$ [*Kuik et al*., 1988], which we refer to as the deep water wave parameters). Wind speeds and directions were measured at position 7a, 10 m above mean sea level. Surveys of the local bathymetry were conducted every few days, see *Ruessink et al*. [2000] for more details.

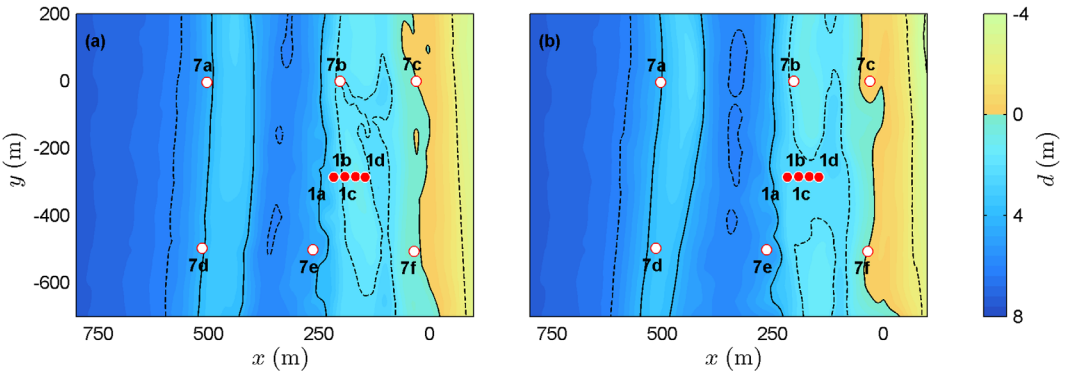

Figure 1. Plan view of the local bathmetry, relative to the mean sea level and in local coordinates, at the Egmond field site for (a) 24 October 1998 and (b) 12 November 1998. A red circle with white filling indicates a pressure sensor (gauges 7a–7f) and a white circle with red filling indicates a collocated bidirectional current meter and pressure sensor (gauges 1a–1d). The black lines (solid and dashed) are depth contours.

A wide range of conditions was encountered during the 2 month experiment. The significant wave height ranged 0.2–5.2 m, the peak period ranged 2.1–11.1 s, and the mean-wave direction varied between $\pm 45^{\circ}$ (relative to the shore normal). The neap and spring tidal range was approximately 1.4 and 2.1 m, respectively. Alongshore variations in the bathymetry were relatively small for most of October. However, on 29 October a broad cross-shore channel developed near the location of the measurement transect (Figure 1b) [*Ruessink et al*., 2001].

In this study, we analyzed measurements and predictions for relatively mild ($H_{m_0,d} \leq 1.5$ m), moderate (1.5 m $< H_{m_0,d} \leq 3$ m), and severe wave conditions ($H_{m_0,d} > 3$ m), belonging to two consecutive storm events. The first event (E1) corresponds to the most severe storm encountered during the experiment (25–29 October), and the second event (E2) corresponds to a storm that occurred after the development of the cross-shore channel (5–7 November). In the tables of this paper, we distinguish between the six cases using a code (e.g., E1a), which indicates the event (E1 or E2), and the wave condition (mild, a; moderate, b; or severe, c).

2.2. Numerical Model

Over the past years, nonhydrostatic models have become an increasingly popular tool to simulate wave-flow dynamics on a variety of scales. Applications range from the evolution of waves at coastal scales [e.g., *Zijlema and Stelling*, 2008; *Yamazaki et al*., 2009; *Ma et al*., 2012; *Ai and Jin*, 2012; *Cui et al*., 2012; *Wei and Jia*, 2014] to the evolution of tsunami waves at oceanic scales [e.g., *Walters*, 2005; *Yamazaki et al*., 2011]. Furthermore, several authors have improved the efficiency of the nonhydrostatic approach [e.g., *Bai and Cheung*, 2012, 2013; *Cui et al*., 2014]. In this study, we use the open-source nonhydrostatic wave-flow model SWASH to simulate the nearshore wave dynamics at the field site. SWASH has been successfully used to study various nearshore processes under laboratory conditions. This includes the nearshore evolution of short waves [*Zijlema et al*., 2011], the nearshore evolution of infragravity waves [*Rijnsdorp et al*., 2014], the depth-induced breaking of short waves [*Smit et al*., 2013], the nonlinear wave dynamics in the surf zone [*Smit et al*., 2014], and runup oscillations [*Ruju et al*., 2014]. Here a brief description of the numerical model is given. A comprehensive description of the model can be found in *Zijlema et al*. [2011] and *Smit et al*. [2013].

2.2.1. Governing Equations and Numerical Implementation

SWASH is based on the Reynolds-averaged Navier-Stokes equations for an incompressible flow with constant density. We consider a three-dimensional domain that is vertically bounded by a free surface $z=\zeta(x,y,t)$ and a bottom $z=-d(x,y)$, where t is time, and x, y, and z are the Cartesian coordinates ($z=0$ is still water level). In this framework, using the Einstein summation convention for the horizontal coordinates, the governing equations are,

$$\frac{\partial u_j}{\partial x_j}+\frac{\partial w}{\partial z}=0, \tag{1}$$

$$\frac{\partial u_i}{\partial t}+\frac{\partial u_i u_j}{\partial x_j}+\frac{\partial u_i w}{\partial z}=-\frac{1}{\rho}\frac{\partial (p_h+p_{nh})}{\partial x_i}+\frac{\partial \tau_{ij}}{\partial x_j}+\frac{\partial \tau_{iz}}{\partial z}, \tag{2}$$

$$\frac{\partial w}{\partial t}+\frac{\partial w u_j}{\partial x_j}+\frac{\partial w^2}{\partial z}=-\frac{1}{\rho}\frac{\partial (p_h+p_{nh})}{\partial z}+\frac{\partial \tau_{zj}}{\partial x_j}+\frac{\partial \tau_{zz}}{\partial z}-g, \tag{3}$$

where subscripts i and j refer to the two horizontal coordinates, u_i is the velocity component of $\vec{u}$ in the i direction, w is the vertical velocity component, g is the gravitational acceleration, ρ is the density, τ is the turbulent stress, p_h is the hydrostatic pressure, and p_{nh} is the nonhydrostatic pressure. An expression for the free surface is derived by considering the mass balance over the entire water column,

$$\frac{\partial \zeta}{\partial t}+\frac{\partial}{\partial x_j}\int_{-d}^{\zeta} u_j dz=\frac{\partial \zeta}{\partial t}+\frac{\partial h_j U_j}{\partial x_j}=0, \tag{4}$$

where $h(=d+\zeta)$ is the total water depth.

At the bottom boundary, turbulence is assumed to be generated by bottom friction,

$$\tau_{iz}|_{z=-d}=c_f\frac{U_i|\vec{U}|}{h}, \tag{5}$$

where c_f is a dimensionless friction coefficient. *Feddersen et al*. [1998] found that c_f is enhanced inside the surf zone due to breaking waves. We computed c_f using the Manning-Strickler formulation, $c_f=gn^2/h^{1/3}$, where n is the Manning roughness coefficient. This formulation gives increasing c_f values for decreasing depth, which makes it a suitable proxy to mimic the wave breaking enhanced c_f. In this study, n was set at $0.019\,s/m^{1/3}$, which results in c_f values of similar order of magnitude as found on a sandy beach [e.g., *Feddersen et al*., 1998, 2003; *Ruessink*, 2010]. The turbulent stresses are based on a turbulent viscosity approximation. For example, the horizontal stresses are given by $\tau_{ij}=\nu_j\partial_{x_j}u_i$, where ν_j is the eddy viscosity. In this study, the horizontal viscosities were estimated using a Smagorinsky-type formulation [e.g., *Smit et al*., 2013]. To include vertical mixing, the vertical viscosity was set at a constant value (10^{-4} m^2/s). This spreads the effect of the bottom stress term over the vertical and may improve the numerical stability.

The governing equations intrinsically account for the processes governing the nearshore (infragravity) wave evolution. However, the numerical methods used to discretize these equations, and the spatial and temporal resolution used in a simulation determines the accuracy with which these processes are resolved. In contrast with traditional nonhydrostatic models [e.g., *Casulli and Stelling*, 1998], the numerical schemes used in SWASH to approximate the nonhydrostatic pressure terms allow the model to resolve the nearshore wave evolution with a relatively coarse vertical resolution [*Stelling and Zijlema*, 2003] (1–3 layers versus 10–20 layers for the traditional approach). This allows model applications at relatively large horizontal scales. Consequently, SWASH captures the relevant physics in the nearshore (e.g., refraction, diffraction, shoaling, and nonlinear interactions) with only a few vertical layers. In this study, two vertical layers were employed.

The model also captures the bulk dissipation of a breaking wave, without the need to resolve detailed phenomena such as wave overturning [*Smit et al*., 2013]. However, a fine vertical resolution (10–20 layers) is usually required to capture the initiation of wave breaking, which is not feasible for the horizontal scales considered in this study. Instead, we used the hydrostatic front approximation that was implemented by *Smit et al*. [2013] to capture the onset of breaking with two layers. With this approximation, the nonhydrostatic pressure is neglected in the vicinity of a breaking wave, which ensures that the wave develops a vertical face (see *Smit et al*. [2013] for more details). This breaking formulation requires a breaking threshold (controlling the onset of wave breaking) and a breaking persistence parameter, which were set to the values found by *Smit et al*. [2013] for two vertical layers.

2.2.2. Model Setup

The horizontal coordinates correspond to a local coordinate system, with the x axis positioned perpendicular to the shore and the y axis positioned parallel to the shore. A schematic view of the numerical domain is presented in Figure 2. At the offshore boundary (the western boundary in Figure 2), incident waves were

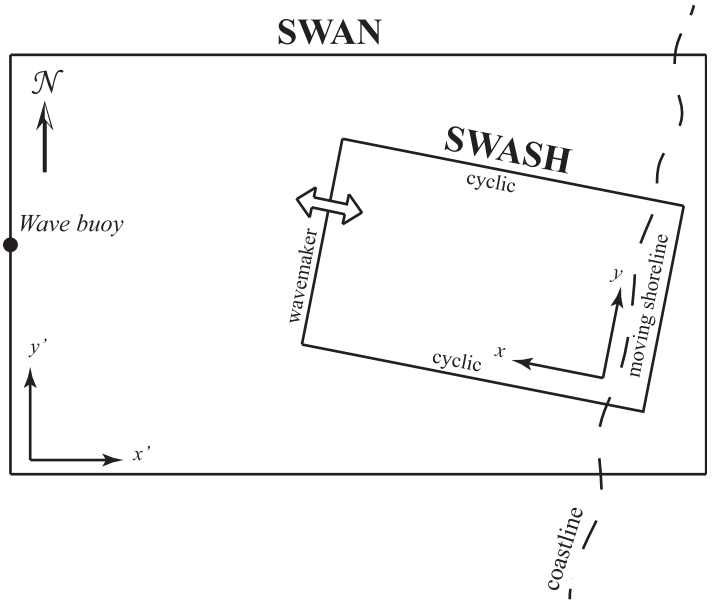

Figure 2. Sketch of the SWASH model domain and the SWAN model domain (not to scale).

generated using weakly nonlinear wave theory, based on a target wave spectrum. The target spectrum represents a directional random wavefield, which is formed by a superposition of a large number of free wave components. Each wave component represents a linear (long-crested) harmonic wave, with a certain amplitude, period, direction, and phase. The target spectrum was obtained with the spectral wave model SWAN [*Booij et al.*, 1999], based on wave data measured by a buoy located 5 km offshore (see Figure 2). A description of the numerical wavemaker and the computation of the target wave spectrum is given in Appendices A–C. At the shore (the eastern boundary in Figure 2), a moving-shoreline boundary condition was employed to accurately simulate wave runup and flooding and drying [*Stelling and Duinmeijer*, 2003]. At the lateral boundaries (the northern and southern boundaries), a cyclic boundary condition was prescribed to simulate the fluid motion on an unbounded beach.

A bathymetry was constructed for the first storm event, based on local survey data obtained on 24 October, and for the second storm event, based on local survey data obtained on 12 November. Figure 1 shows a plan view of the constructed bathymetry for both storm events. To construct a cyclic bathymetry in y direction, the bathymetry was extended from $y = -700$ m to $y = -1100$ m, with a linear transition between the cross-shore profile at the northern boundary ($x = 200$ m) and at $y = -700$ m. The resulting numerical domain spanned 1400 $\times$ 1300 m ($x \times y$) for mild to moderate wave conditions, and 2150 $\times$ 1300 m for severe conditions. This includes a region of constant depth at the western boundary, with a maximum depth of 15 m for the severe conditions, and 10 m for the mild and moderate conditions.

Table 1 shows an overview of the SWAN predicted bulk wave parameters, with which SWASH was forced. To accurately capture the characteristics of the dominant wavefield, a grid resolution was chosen that ensured at least 15 points per wave length for waves up to $3f_p$, where f_p is the peak frequency of the target spectrum. This resulted in horizontal grid resolutions that varied between $\Delta x = 0.5-1$ m, and $\Delta y = 0.8-1.4$ m, depending upon the simulation. To resolve the dispersion of waves up to $3f_p$, two vertical layers were used. The time step ranged $\Delta t = 0.02-0.03$ s. At the numerical wavemaker, the nonlinearity of the wavefield should be small, as the wavemaker is based on weakly nonlinear wave theory. We quantified the nonlinearity using the Ursell number, based on the target bulk parameters (Table 1) and the depth at the wavemaker. The Ursell number ranged 3–16, which is acceptable for the application of the numerical wavemaker [e.g., *Holthuijsen*, 2007].

Table 1. Target Bulk Wave Parameters at the Numerical Wavemaker, Computed With SWAN[a]

	H_{m_0} (m)	T_p (s)	$\bar{\theta}$ (°)	$\bar{\sigma}_\theta$ (°)
E1a	1.2	6.1	35	21
E1b	2.2	7.8	29	21
E1c	4.7	10	−1	27
E2a	1.5	6.5	−15	22
E2b	1.9	7.4	3	24
E2c	3.7	8.7	−3	27

[a]Listed are the wave height $H_{m_0} (=4\sqrt{\int E(f)df}$, where $E(f)$ is the SWAN predicted variance density spectrum), the peak period T_p, the energy-weighted mean-wave direction $\bar{\theta}$, and the energy-weighted directional spreading $\bar{\sigma}_\theta$. Wave directions are related to the local coordinate system, where $\bar{\theta} = 90^\circ$ corresponds to northerly waves and $\bar{\theta} = -90^\circ$ corresponds to southerly waves.

For each simulation, the model was run for 1 h and 20 min, including 20 min of spin-up time. Model variables (ζ, u, and v) were

output with a sampling rate of 4 Hz, at the measurement devices and at 66 cross-shore transects. These transects spanned the whole model domain with a resolution of 5 m in x direction, and 20 m in y direction.

2.3. Data Analysis

We distinguished between wind-generated waves and infragravity waves by defining two frequency bands, one representing the infragravity waves ($0.005\,\mathrm{Hz} < f \leq f_p/2$), and one representing the short waves ($f_p/2 < f \leq 3f_p$). These two adjacent bands are separated by a split frequency of $f_p/2$, which is similar to several previous studies [e.g., *Janssen et al*., 2003; *Pomeroy et al*., 2012]. These frequency bands were used to decompose the surface elevation and velocity signals into an infragravity and short-wave component. In the following analyses, an infragravity-wave signal is indicated by a tilde (˜), and a short-wave signal is indicated by a prime ($'$).

2.3.1. Model-Data Comparison

To facilitate a model-data comparison, several parameters were computed for the model predictions and observations, using the same techniques and based on signals of equal length (34 min, the length of the observed signals). All (co)spectra in this section were computed with 30 degrees of freedom, based on ensemble-averaged Fourier transforms of detrended and windowed time signals.

Significant wave heights were computed as $H_{m_0} = 4\sqrt{m_0}$, where $m_0 \left(= \int E(f) df\right)$ is the zeroth-order moment of the energy density spectrum $E(f)$ of the surface elevation. Infragravity and short-wave heights were computed by integrating spectra over their respective frequency bands. Directional properties, the mean-wave direction $\theta(f)$ and directional spreading $\sigma_\theta(f)$, were computed following *Kuik et al*. [1988], based on second-order Fourier directional moments. Bulk short-wave directional properties were computed using an energy-weighted integration over the short-wave frequencies [e.g., *Feddersen et al*., 2011].

To compare the predicted and observed nearshore energy losses of infragravity waves, bulk-infragravity reflection coefficients were computed based on cross-shore directed linear energy fluxes of shoreward and seaward-propagating infragravity waves (superscript $\pm$, respectively), using the technique of *Sheremet et al*. [2002]. Linear energy fluxes follow from collocated surface elevation and cross-shore directed velocity signals, assuming that the infragravity waves are shore-normal propagating shallow-water waves,

$$F_L^{\pm}(f) = \frac{1}{4}\sqrt{gd}\left(C_f(\zeta,\zeta) + \frac{d}{g}C_f(u,u) \pm 2\sqrt{\frac{d}{g}}C_f(\zeta,u)\right), \tag{6}$$

where C_f(X, Y) represents the cospectrum between the real signals $X(t)$ and $Y(t)$. The frequency-dependent reflection coefficient is defined as the ratio of the seaward to the shoreward flux. Integrating fluxes over the infragravity frequencies yielded estimates of the bulk-infragravity reflection coefficient, $R^2 = F_L^- / F_L^+$, where $F_L^{\pm}$ is the linear flux integrated over the infragravity frequencies. *Sheremet et al*. [2002] estimated that errors in $F_L^{\pm}$ and R^2, because of the normal incidence assumption, were smaller than 20%.

2.3.2. Infragravity-Wave Dynamics

Analyses of the infragravity-wave dynamics were based on 1 h long model results—which is longer than the 34 min measured signals. All the (wave number) frequency (co)spectra in this section were computed with 30 degrees of freedom.

In the nearshore, the wave-flow field at the infragravity frequencies is composed of irrotational (e.g., leaky and edge waves) and rotational motions (e.g., eddies generated by wave group forcing [e.g., *MacMahan*, 2004; *Reniers et al*., 2007], eddies generated by individual wave crests [*Clark et al*., 2012; *Feddersen*, 2013], and instabilities of the longshore current [e.g., *Özkan Haller and Kirby*, 1999]). The simultaneous occurrence of these phenomena makes it impossible to identify the presence of leaky and edge waves without alongshore information. However, leaky and edge waves can be identified using the alongshore-wave number frequency spectra, based on their alongshore wave number ($\kappa[m^{-1}]$) and frequency combination. In this study, alongshore-wave number frequency spectra $E(\kappa, f)$ were computed for surface elevation and velocity signals, which covered the whole numerical domain in y direction.

To quantify the contribution of leaky and edge waves to the local infragravity-wave field, we partitioned the energy in the $E(\kappa, f)$ into two bands: a leaky-wave band and an edge-wave band. A free infragravity wave was considered leaky if its $\kappa - f$ combination can exist at the numerical wavemaker, that is, if

$\kappa_l < \pm f/\sqrt{gd_0}$, where d_0 represents the still water depth at the wavemaker. If the κ is larger than this limit, the free wave cannot exist at the offshore boundary and is trapped shoreward of the wavemaker. At relatively large κ, gravity waves do not exist and only rotational motions occur. To exclude these rotational motions from this analysis, the lower limit of the edge-wave band corresponded to a zero-mode edge wave on a plane beach [e.g., *Howd et al.*, 1991], $\kappa_0 = \pm f^2/(g\beta)$, where $\beta(=1/100)$ is the local beach slope. Although this analysis does not differentiate between (incoming) bound and free infragravity waves, it does indicate the relative importance of leaky versus trapped motions, because the alongshore wave number of a shoreward directed bound infragravity wave dictates whether its reflection will be trapped nearshore (assuming an alongshore uniform beach). The contributions of both bands were quantified at each cross-shore location by integrating the energies over their respective bands,

$$E_{\mathrm{ig,leaky}}(x) = \int_{f_{\mathrm{lo}}}^{f_{\mathrm{hi}}} \int_{-\kappa_l - \Delta\kappa_l}^{\kappa_l + \Delta\kappa_l} E(\kappa, f, x)\, d\kappa df, \tag{7}$$

$$E_{\mathrm{ig,edge}}(x) = \int_{f_{\mathrm{lo}}}^{f_{\mathrm{hi}}} \int_{-\kappa_0 - \Delta k_0}^{\kappa_0 + \Delta\kappa_0} E(\kappa, f, x)\, d\kappa df - E_{\mathrm{ig,leaky}}(x), \tag{8}$$

in which the frequency limits follow from the infragravity frequency band (f_{lo}=0.005 Hz, and $f_{\mathrm{hi}} = f_p/2$). The constant wave number offsets, $\Delta\kappa_l$, and $\Delta\kappa_0$, account for the variation of κ in a frequency bin. Following *Oltman-Shay and Guza* [1987], these offsets were estimated as the derivative of their respective dispersion relationship, $\Delta\kappa_l = \Delta f/\sqrt{gd_0}$, and $\Delta\kappa_0 = 2f\Delta f/(g\beta)$, respectively.

Besides estimating the energies in the leaky and edge-wave band, we estimated the contribution of bar-trapped edge waves to the local infragravity-wave field. Theoretically, edge waves are trapped at a bar if $f\sqrt{gd^*_{\mathrm{trough}}} \le \kappa \le f\sqrt{gd^*_{\mathrm{bar}}}$ [e.g., *Bryan et al.*, 1998], where d^*_{bar} and d^*_{trough} indicate the effective depth at the bar and in the trough, respectively, which includes the effect of the alongshore current [*Howd et al.*, 1992]. Furthermore, they are characterized by a relatively large amplitude near a local minima in the depth profile (e.g., bars), and an exponentially decreasing amplitude away from this location. Based on these characteristics, the contribution of bar-trapped edge waves to the local infragravity-wave field was estimated by integrating the energies over the $\kappa - f$ combinations that satisfy the theoretical limits (including wave number offsets), but only if its energy is amplified relative to the shore. The amplification was computed as,

$$A(\kappa, f, x) = \frac{E(\kappa, f, x)}{E^{\mathrm{ref}}(\kappa, f)}, \tag{9}$$

where $E^{\mathrm{ref}}(\kappa, f)$ is a reference spectrum, which was taken at an alongshore transect near the shoreline ($d \approx 1$ m). Energies were considered to represent bar-trapped edge waves if $A(\kappa, f, x) \ge 5$, to exclude relative small amplifications from the estimation.

The wave number frequency spectra of the surface elevation signal were decomposed in shoreward and seaward directed contributions using the technique proposed by *Sheremet et al.* [2005]. This technique, based on WKB theory (which assumes small depth variations), yields estimates of the linear energy fluxes in a $\kappa - f$ region that is bounded by the shallow-water phase velocity ($\kappa = f/\sqrt{gd}$). These fluxes are defined as,

$$F_L^{\pm}(\kappa, f) = \frac{d}{4}\left(\frac{|c_x|}{d} C_{\kappa,f}(\zeta, \zeta) \pm 2C_{\kappa,f}(\zeta, u) + \frac{d}{|c_x|} C_{\kappa,f}(u, u)\right), \tag{10}$$

where c_x is the cross-shore component of the shallow-water phase velocity, and $C_{\kappa,f}(X, Y)$ is the cospectrum in $\kappa - f$ space between the real signals $X(y, t)$ and $Y(y, t)$.

To analyze the relationship between the wave groups and the infragravity waves, we evaluated the steady, weakly nonlinear infragravity energy balance, following *Henderson et al.* [2006]. Here we used an extension of the original method, removing the assumptions of (near) shore-normal short-wave propagation and alongshore uniformity,

$$\frac{\partial F_x(f)}{\partial x} + \frac{\partial F_y(f)}{\partial y} = W(f) - D_b(f), \tag{11}$$

where $F_x(f)$ and $F_y(f)$ are the cross-shore and alongshore directed energy flux, $D_b(f)$ is a dissipation term representing bottom friction, and $W(f)$ represents a nonlinear energy transfer at infragravity frequency f. The energy fluxes are a combination of a linear $F_L(f)$ and a nonlinear contribution $F_{NL}(f)$,

$$F_x(f)=gdC_f\left(\tilde{\zeta},\tilde{u}\right)+gC_f\left(\tilde{\zeta},M\right)\equiv F_{L,x}(f)+F_{NL,x}(f), \tag{12}$$

$$F_y(f)=gdC_f\left(\tilde{\zeta},\tilde{v}\right)+gC_f\left(\tilde{\zeta},N\right)\equiv F_{L,y}(f)+F_{NL,y}(f), \tag{13}$$

where $M(=\zeta' u')$, and $N(=\zeta' v')$ represent mass fluxes in x and y direction, respectively.

The nonlinear transfer term is defined as,

$$W(f)=-C_f\left(\tilde{u},\frac{\partial S_{xx}}{\partial x}\right)-C_f\left(\tilde{u},\frac{\partial S_{xy}}{\partial y}\right)-C_f\left(\tilde{v},\frac{\partial S_{xy}}{\partial x}\right)-C_f\left(\tilde{v},\frac{\partial S_{yy}}{\partial y}\right), \tag{14}$$

where $S_{xx}\left(=du'u'+\frac{1}{2}g\zeta'\zeta'\right)$, $S_{xy}(=du'v')$, and $S_{yy}\left(=dv'v'+\frac{1}{2}g\zeta'\zeta'\right)$ are the radiation stress terms. An alternative, but mathematically equivalent, expression for the nonlinear energy transfer term can be derived by rewriting the gradient terms $\left(\text{e.g.,}\,\tilde{u}\frac{\partial S_{xx}}{\partial x}=\frac{\partial \tilde{u}S_{xx}}{\partial x}-\frac{\partial \tilde{u}}{\partial x}S_{xx}\right)$. Although these terms are mathematically equivalent, differences may arise when evaluating the derivatives if the spacing between two discrete points is too large [e.g., *Péquignet et al*., 2014]. A sensitivity study indicated that a 5 m output spacing in x direction, and a 20 m output spacing in y direction yielded similar results for both expressions, which was therefore chosen to be the output resolution (see section 2.2.2). The gradients were evaluated using central differences.

Bulk flux and transfer terms were computed by integrating the terms over the infragravity frequency band. In this study, we only considered the bulk effect of the dissipation due to bottom friction, which was computed following [*Henderson and Bowen*, 2002],

$$D_b=c_f\left(\overline{u^2+v^2}\right)^{\frac{1}{2}}\overline{\tilde{u}^2+\tilde{v}^2}, \tag{15}$$

where the overbar denotes an averaging operation. This expression results from a bottom stress parameterization that is equivalent to the bottom stress formulation used in the SWASH model. To evaluate this term consistent with the simulations, the dimensional friction coefficient c_f was computed following the Manning-Strickler formulation used in the simulations (see section 2.2.1).

In this work, we present the infragravity energy balance throughout the nearshore in terms of alongshore-averaged bulk parameters, and frequency varying parameters. These terms were first computed along each cross-shore transect, excluding the extended part of the numerical domain, after which they were averaged in alongshore direction. For all conditions considered in this study, contributions of rotational motions to the energies at the infragravity frequencies (computed following *Lippmann et al*. [1999]) did not exceed 55%.

3. Results: Model-Data Comparison

Before analyzing the infragravity-wave dynamics based on the model results, we assessed the ability of SWASH to produce a wavefield that is representative for the natural conditions at the field site. For this purpose, we compared predictions and observations of six bulk parameters, and three frequency-dependent wave parameters.

3.1. Bulk Parameters

First, we discuss comparisons between predictions and observations of six bulk parameters: the significant short-wave height ($H_{m_0,s}$), the significant infragravity-wave height ($H_{m_0,ig}$), the energy-weighted mean short-wave angle ($\bar{\theta}$), the energy-weighted short-wave directional spread ($\bar{\sigma}_\theta$), the alongshore current (V), and the bulk-infragravity reflection coefficient (R^2).

Model predicted $H_{m_0,s}$ agreed with the observations, which is illustrated by the results of the four wave conditions shown in Figures 3a–3d. The results of these wave conditions were representative for all conditions, as illustrated by the error and skill measures (Table 2). Predicted $H_{m_0,ig}$ were of similar order of magnitude

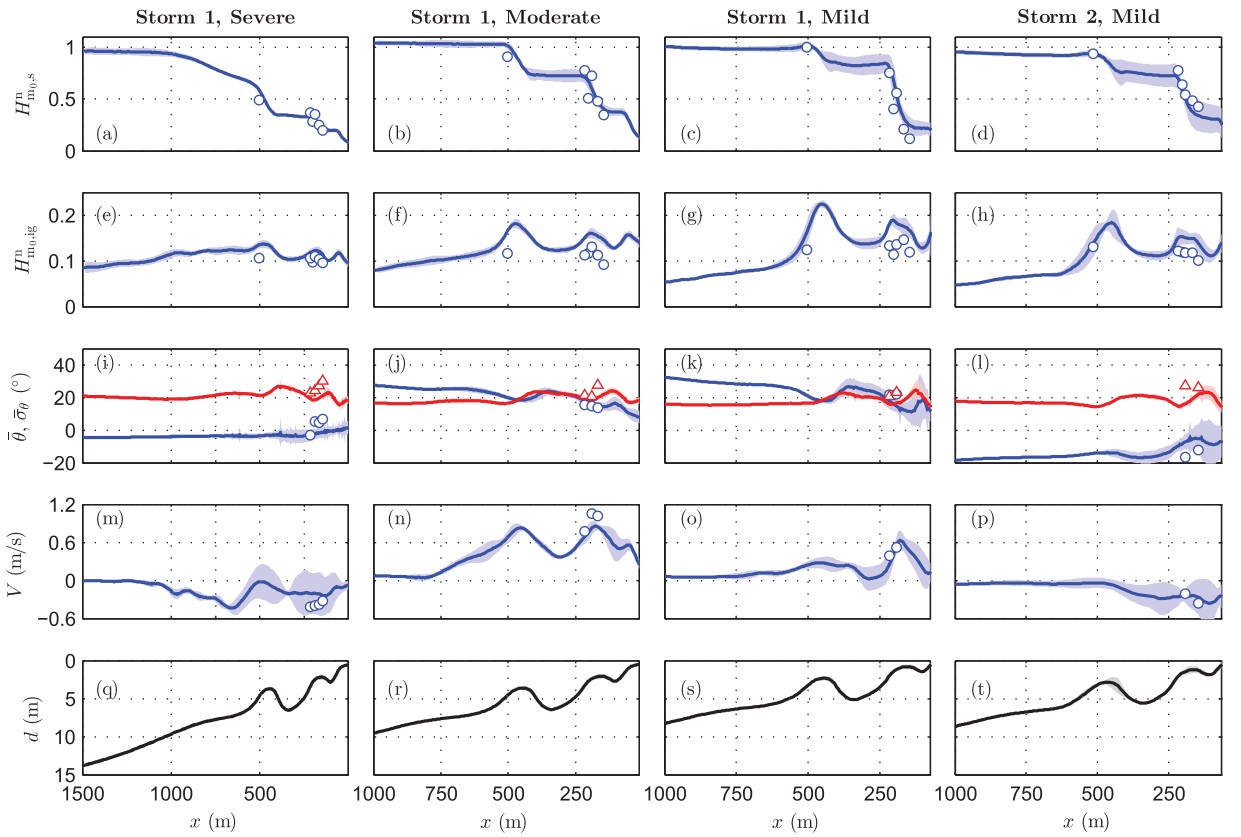

Figure 3. (a–d) Measured (symbols) and predicted (alongshore mean, lines; alongshore standard deviation, shade) normalized significant short-wave height $H^n_{m_0,s}$; (e–h) normalized significant infragravity-wave height $H^n_{m_0,ig}$; (i–l) mean short-wave direction $\bar{\theta}$ (blue line and blue circles), and short-wave directional spread $\bar{\sigma}_\theta$ (red line and red triangles); and (m–p) longshore current V for four wave conditions. The wave heights were normalized with the target wave height (see Table 1). (q–t) The depth (alongshore mean, lines; alongshore standard deviation, gray shade).

as the observations (Table 2), although $H_{m_0,ig}$ was generally over predicted at the gauge locations (Figures 3e–3h). For the four wave conditions shown in Figures 3e–3h, the predicted $H_{m_0,ig}$ had a striking cross-shore evolution: a local maximum occurred near the crest of the outer bar ($x \approx 450$ m), and near the crest of the inner bar ($x \approx 200$ m). Such patterns were also observed for the moderate to severe wave conditions of the second storm event (not shown). These maxima were most pronounced for the low energetic wave conditions (Figures 3g and 3h). We will return to these features in section 4.1.

Table 2. Root-Mean-Square Error (RMSE) and Skill Factor of the Significant Short-Wave Height ($H_{m_0,s}$) and Infragravity-Wave Height ($H_{m_0,ig}$), Computed for All Gauges With Available Surface-Elevation Measurements, and the Bulk-Infragravity Reflection Coefficient (R^2), Computed for All Gauges With Available Surface-Elevation and Velocity Measurements[a]

	E1a	E1b	E1c	E2a	E2b	E2c	Average
RMSE $H_{m_0,s}$	0.04	0.13	0.27	0.14	0.21	0.08	0.14
RMSE $H_{m_0,ig}$	0.06	0.10	0.09	0.05	0.07	0.09	0.08
RMSE $\bar{\theta}$	2.49	1.22	4.98	0.78	2.88	2.67	2.50
RMSE $\bar{\sigma}_\theta$	2.82	3.73	4.66	5.27	2.40	5.56	4.07
RMSE V	0.17	0.11	0.03	0.05	0.04	0.07	0.08
RMSE R^2	0.03	0.06	0.20	0.12	0.06	0.08	0.09
Skill $H_{m_0,s}$	0.95	0.91	0.82	0.86	0.81	0.96	0.88
Skill $H_{m_0,ig}$	0.60	0.61	0.81	0.72	0.69	0.77	0.70
Skill $\bar{\theta}$	0.56	0.68	−0.40	0.72	0.13	0.23	0.32
Skill $\bar{\sigma}_\theta$	0.72	0.80	0.72	0.95	0.92	0.84	0.83
Skill V	0.37	0.83	0.91	0.71	0.72	0.52	0.68
Skill R^2	0.91	0.87	0.46	0.61	0.73	0.83	0.74

[a]Results are listed for each wave condition, and averaged over all conditions. For quantity Q, the RMSE was computed as, $\text{RMSE}=\sqrt{\langle(Q_p-Q_o)^2\rangle}$, and the skill factor was computed as, $\text{Skill}=1-\sqrt{\langle(Q_p-Q_o)^2\rangle/\langle Q_o^2\rangle}$, where $\langle\ldots\rangle$ indicates averaging over the available gauges, and subscript o and p indicate observed and predicted values, respectively.

Table 3. Measured and Predicted Bulk-Infragravity Reflection Coefficients (R^2) at Gauge 1b

	E1a	E1b	E1c	E2a	E2b	E2c
Measured	0.37	0.37	0.33	0.33	0.25	0.41
Predicted	0.33	0.40	0.14	0.25	0.17	0.39

Differences between the observed and measured bulk short-wave direction ($\bar{\theta}$) were on average 2.5° (Figures 3i–3l and Table 2). Although the absolute error was only a few degrees, predicted $\bar{\theta}$ had a relatively low skill. The skill was even negative for the severe condition of the first storm, for which predicted and observed $\bar{\theta}$ were of different sign at some sensors (see Figure 3i). Errors were partly due to inaccuracies in $\bar{\theta}$ observations, which were of $\mathcal{O}(1^\circ)$, resulting in relatively large measurement inaccuracies in case of nearshore normal mean-wave angles (e.g., Figure 3i). Measurements of the directional spreading $\bar{\sigma}_\theta$ were more reliable than $\bar{\theta}$. For all conditions, predicted $\bar{\sigma}_\theta$ were smaller than the observations, with an average error of 4°, which corresponds to an average skill of 0.83 (Table 2). These over predictions of $\bar{\sigma}_\theta$ likely contributed to the over predictions of $H_{m_0,ig}$, as the directional spreading of a short-wave field significantly reduces the bound wave response [e.g., *Okihiro et al.*, 1992].

The direction of the predicted alongshore current V was always consistent with the observations, although errors in magnitude were significant (on average 0.08 m/s, corresponding to a skill of 0.68). Discrepancies were partly caused by the absence of tidal and wind-driven currents in the simulations, because their combined contribution to the alongshore momentum balance in the bar-trough region was equal to approximately 40% of the wave forcing [*Ruessink et al.*, 2001]. Furthermore, the coarse spatial resolution of the velocity sensors complicates a comparison of the spatial structure of V, although the model appears to capture the location of significant alongshore currents near the inner bar for conditions with relatively large incident wave angles (Figures 3n and 3o).

The observed bulk-infragravity reflection coefficients (R^2) indicate that the shoreward directed linear flux component was larger than the seaward directed component at gauge 1b (Table 3), which was the most shoreward located gauge where velocity measurements were available for all wave conditions. At this nearshore location, the nonlinear flux contribution was typically small, and the linear flux dominated the total flux, as exemplified by the model results (see Figure 6). The small R^2 values therefore suggest that a significant part of the infragravity-wave energy was dissipated and/or trapped shoreward of gauge 1b. SWASH reproduced the relatively low R^2 observations with an average skill of 0.74, but typically predicted lower R^2 values compared to the measurements (Tables 2 and 3). This indicates that the model overestimated the nearshore infragravity dissipation and/or trapping.

3.2. Spectral Parameters

Next, we discuss comparisons of predictions and observations of the frequency variation of the reflection coefficient $R^2(f)$, and the frequency spectra of the surface elevation, u-velocity component and v-velocity component. At the inner bar, the observed $R^2(f)$ showed a distinct frequency-dependent behavior, consistent with a previous study at this field site [*de Bakker et al.*, 2014]. For all conditions, $R^2(f)$ was near zero for relatively high frequencies, whereas at lower frequencies $R^2(f)$ indicated near-perfect reflections (Figure 4). The predicted $R^2(f)$ show a similar frequency dependency, although predicted values were typically smaller than the observations, consistent with the bulk R^2 (Table 3). At the most offshore located gauge (7a or 7d), the predicted spectral shape approximately represented the measurements at the dominant short-wave

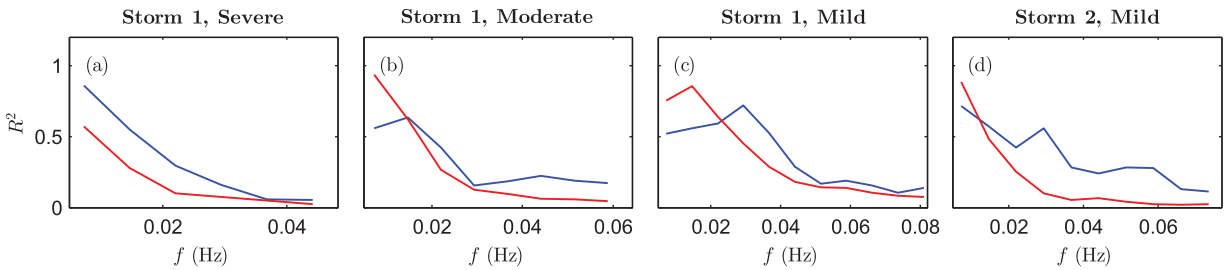

Figure 4. Measured (blue line) and predicted (red line) infragravity reflection coefficient $R^2(f)$ at gauge 1b (located at the inner bar), for four wave conditions.

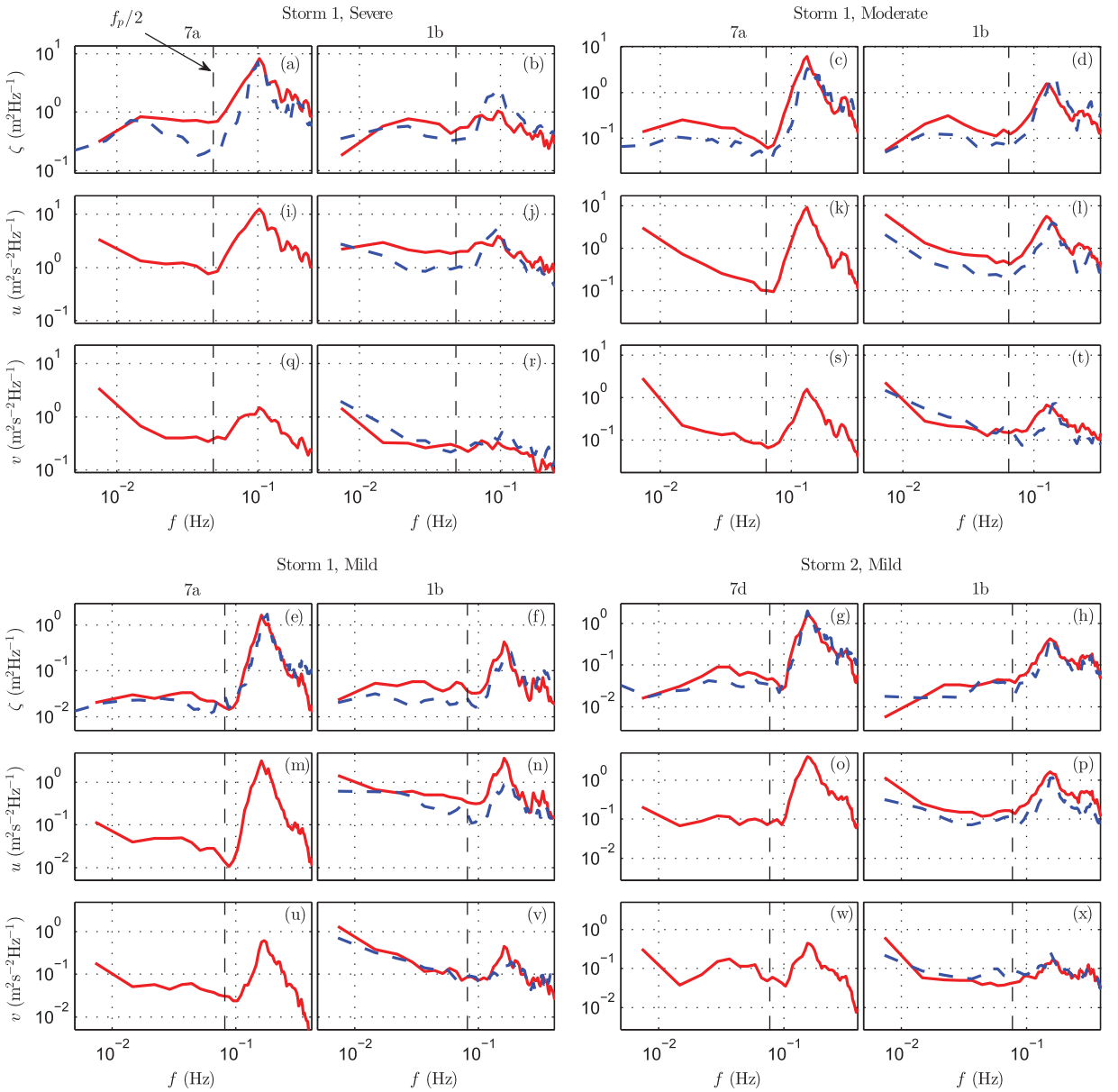

Figure 5. Measured (dashed blue line) and predicted (full red line) frequency spectra of the surface elevation, *u*-velocity component, and *v*-velocity component at the most offshore located operating gauge (Storm 1, 7a; Storm 2, 7d) and at gauge 1b (located at the inner bar), for four wave conditions.

frequencies (Figures 5a, 5c, 5e, and 5g). Near the inner bar, short-wave energies were lower due to wave breaking, and the model qualitatively reproduced the spectral shape for most conditions (Figures 5d, 5f, and 5h), except for the severe condition of the first storm (Figure 5b). At the infragravity frequencies, spectra were relatively broad due to the limited length of the signals (34 min), which complicates a detailed comparison. Infragravity energies were typically overpredicted, as previously observed for $H_{m_0,ig}$. For some conditions, the predicted spectral shape at the infragravity frequencies was broader compared to the measurements (e.g., Figures 5a and 5b), whereas for other conditions the predicted spectral shape resembled the measured shape (e.g., Figures 5c and 5d). Differences at the infragravity frequencies were typically larger if the prediction of the short-wave spectral shape was relatively poor (e.g., Figures 5a and 5b). The spectral shape of the observed *u* and *v* velocity spectra is similar to the surface elevation spectra at most frequencies, except at relatively low infragravity frequencies. At these lower frequencies, energies are relatively large compared to the higher frequencies, which is not reflected in the surface elevation spectra. This is likely due to the presence of rotational motions (e.g., eddies), which have a small contribution to the surface

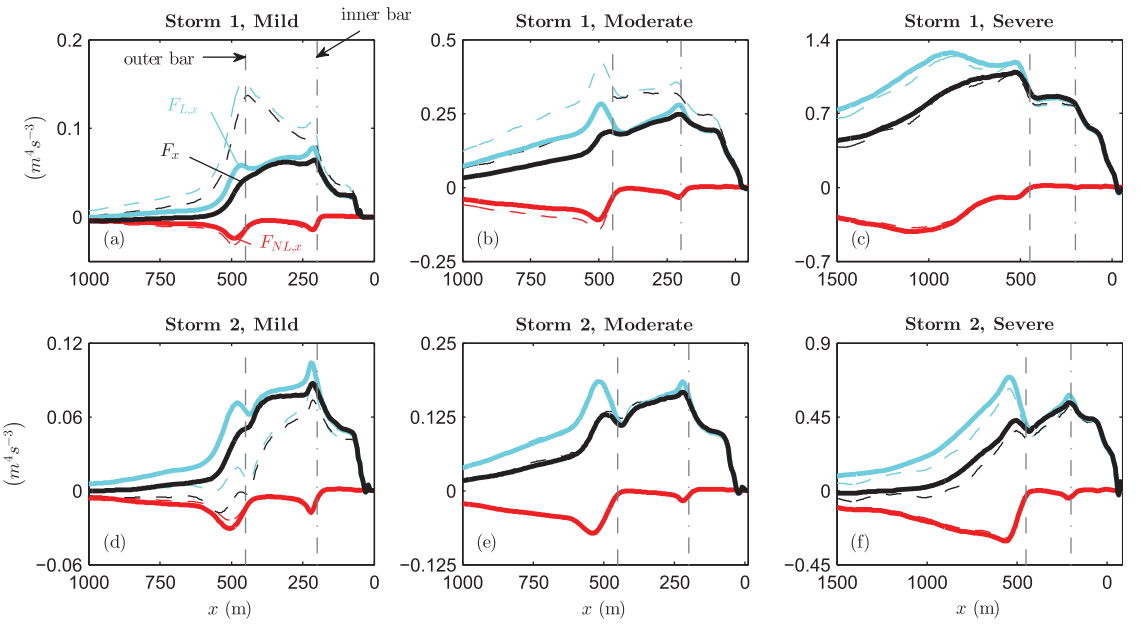

Figure 6. Cross-shore variation of the cross-shore component of the energy flux $F_x\left(=F_{L,x}+F_{NL,x}\right)$ (black line), linear energy flux $F_{L,x}$ (blue line), and nonlinear energy flux $F_{NL,x}$ (red line), integrated over the infragravity band, for the (a and d) mild, (b and e) moderate, and (c and f) severe wave condition of the (a–c) first and (d–f) second storm event. The thin dashed lines represent the total energy flux contributions, for example, $F\left(=F_{L,x}+F_{NL,x}+F_{L,y}+F_{NL,y}\right)$. In all plots, the thin vertical lines indicate the approximate location of the outer (dashed line) and inner bar (dash dotted line).

elevation spectra [e.g., *Lippmann et al.*, 1999]. The predicted spectral shape of both velocity components is similar to the observations, although energies are generally over predicted (e.g., Figures 5l and 5n).

The above mode-data comparison showed that the predicted directional short-wave field reasonably resembled the measured short-wave field, especially given that SWASH was forced based on bulk wave parameters measured by an offshore wave buoy (see section 2.2.2 and Appendix C). The reasonable skill of the predicted infragravity parameters suggests that the predicted infragravity-wave field was representative for the measured infragravity-wave field. We conclude that the predicted wavefield was representative for the wave conditions that were measured during the field experiment. This suggests that SWASH can be used to study the processes governing the nearshore infragravity-wave evolution.

4. Results: Infragravity-Wave Dynamics

In this section, we examine the variation of the infragravity energy in the nearshore, and identify the contributions of (bar-trapped) edge waves and leaky waves (section 4.1). Next, we evaluate the terms that influence the nearshore infragravity energy balance (section 4.2), including the energy exchange between the short and infragravity waves, and the nearshore dissipation of infragravity waves.

4.1. Infragravity Energy in the Nearshore

The cross-shore component of the energy flux (F_x) varied significantly throughout the nearshore for all conditions (Figure 6). Seaward of the outer bar, F_x abruptly increased for mild wave conditions, whereas the increase was more gradual for more energetic conditions. For all conditions, the linear flux $F_{L,x}$ was positive throughout the domain, had a larger magnitude than the nonlinear flux $F_{NL,x}$, and had a similar cross-shore pattern as F_x. In contrast to the positive linear flux, $F_{NL,x}$ was negative and generally significant seaward of the surf zone, consistent with the presence of bound infragravity waves [e.g., *Péquignet et al.*, 2014]. For all but the severe condition of the first storm, $F_{NL,x}$ peaked near the outer and inner bar, and decreased shoreward of both bars. For the severe condition of the first storm, $F_{NL,x}$ peaked at $x \approx 1000$ m (the approximate location of initial wave breaking, see Figure 3a), and became approximately zero shoreward of the outer bar. For all conditions, the patterns suggest that bound wave contributions decreased when short waves were breaking, which typically occurred near the crest of the outer and inner bar (except for the severe condition of the first storm).

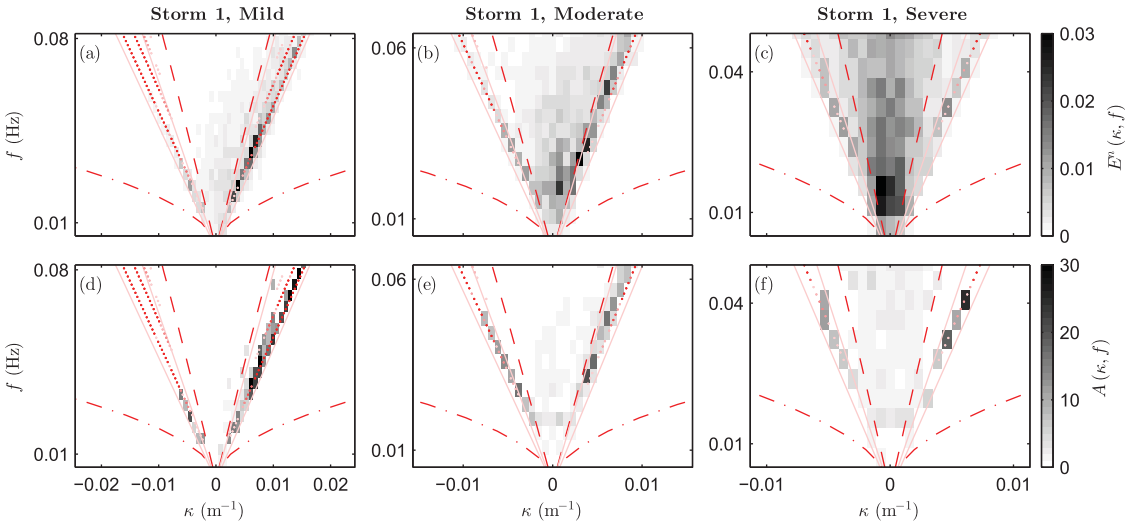

Figure 7. (a–c) Normalized alongshore-wave number frequency spectra of the surface elevation signal $E^n(\kappa, f)$ at the outer bar ($x = 440$ m), and (d–e) ratio $A(\kappa, f)$ of $E(\kappa, f)$ at $x = 440$ m to $E(\kappa, f)$ near the shoreline ($d \approx 1$ m) for the first storm event. The spectra in Figures 7a–7c are normalized with the energy integrated over the infragravity band. In Figures 7d–7f, amplifications with values smaller than one are white. The dashed lines indicate the leaky-wave cutoff, and the dash-dotted line indicates the lowest mode edge-wave dispersion relationship (for a plane beach). The red markers represent numerical predictions of edge-wave modes trapped at the outer bar (following *Howd et al.* [1992]), where the color intensity illustrates the magnitude of the amplification at the outer bar (where the minimum intensity corresponds to an amplification larger than one, and the maximum intensity represents an amplification equal to or larger than 10). The light red lines bound the theoretical region of edge waves that are trapped at the outer bar ($c = \sqrt{g d^*_{\text{bar}}}$, and $c = \sqrt{g d^*_{\text{trough}}}$, where d^*_{bar} and d^*_{trough} indicate the effective depth at the outer bar and in the trough, respectively).

For the mild condition of the first storm event (Figure 6a), the total flux $F\left(=F_x+F_y\right)$ was approximately twice as large as F_x up to the outer bar, indicating that the alongshore flux component F_y was of similar magnitude as F_x. Shoreward of the outer bar, the relative contribution of F_y decreased, and near the shoreline F_x dominated the total energy flux. During the first storm event, the overall contribution of F_y decreased for more energetic conditions, and F_x explained most of the total flux. This is consistent with decreasing incident mean-wave angles for increasingly energetic conditions (Table 1). For the mild condition of the second storm event and the severe conditions of both storm events, the total flux was smaller than F_x, which indicates that the F_y was negative (Figures 6c, 6d, and 6f). We associate these negative F_y values with the dominance of southward over northward-propagating infragravity motions, consistent with the mean angle of wave propagation (Table 1).

The occasional occurrence of significant alongshore directed fluxes near the outer bar suggests that a significant part of the infragravity-wave motion was orientated in alongshore direction, possibly explained by the presence of edge waves. To identify if edge waves indeed contributed to the nearshore infragravity-wave field, we computed alongshore-wave number frequency spectra at various cross-shore locations. Furthermore, edge-wave dispersion curves were computed numerically following the model of *Howd et al.* [1992], based on the (alongshore averaged) bathymetry profile, accounting for the tidal level, and including the influence of the alongshore current. At the outer bar, for the mild wave condition of the first storm event, the surface-elevation spectrum shows a distinct streak of energy at positive κ values, extending from the lower to the higher infragravity frequencies (Figure 7a). The energies at these $\kappa-f$ combinations were significantly larger compared to their values near the shoreline (i.e., $A(\kappa, f) \gg 1$, see Figure 7d). The $\kappa-f$ combinations of these significant amplifications qualitatively agree with numerical predictions of bar-trapped edge-wave modes. These results suggest that edge waves were trapped at the outer bar for this particular wave condition. Most energies were located at positive κ values, which indicates that northward directed waves dominated over southward directed waves, which is consistent with the incident mean-wave direction (Table 1).

The alongshore length of the domain restricts the possible wave modes, as the alongshore domain length is an integer multiple of the alongshore wave length (see Appendix A). This can be observed in Figure 7, as the resolution in κ space is equal to the inverse of the alongshore domain length. Although this restricted the possible infragravity-wave modes, we expect that this did not significantly affect the results as the κ resolution was small ($\Delta\kappa = 1/1300$ m^{-1}), likely resulting in a sufficient number of possible wave modes for the majority of the infragravity frequencies.

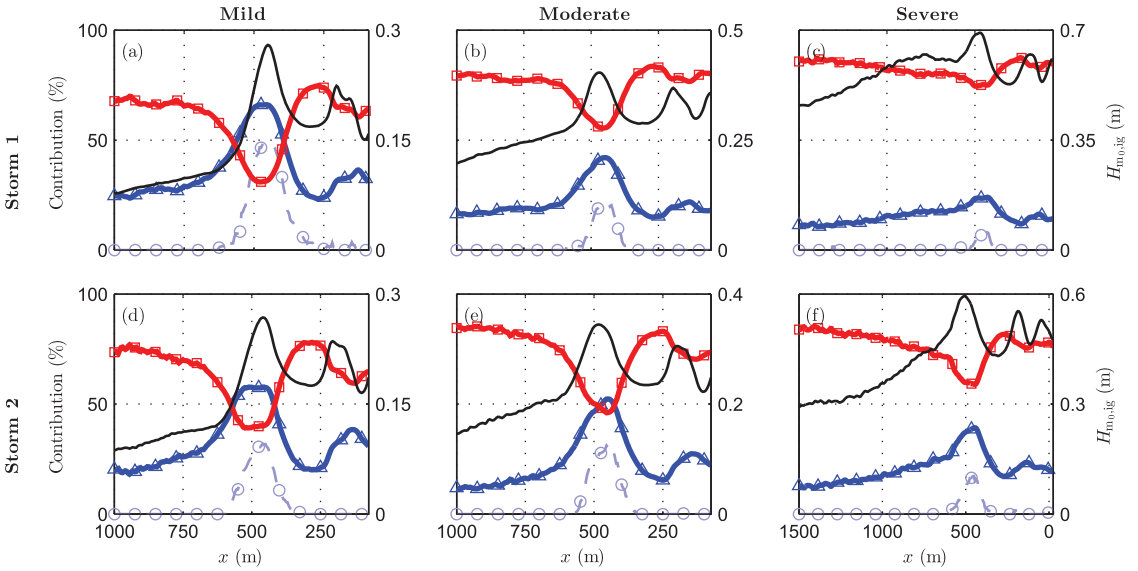

Figure 8. Cross-shore variation of the relative contribution to the surface elevation spectra (in %) of the leaky-wave band (thick red line with square markers), edge-wave band (thick blue line with triangular markers), and bar-trapped edge waves (dashed light-blue line with circle markers). For reference, the black line shows the significant infragravity-wave height (corresponding to the right vertical axis). The top three plots correspond to the (a) mild, (b) moderate, and (c) severe wave condition of the first storm event; and the bottom three plots correspond to the (d) mild, (e) moderate, and (f) severe of the second storm event.

Similar to the mild wave condition, the spectra of the moderate and severe wave condition of the first storm event show a distinct energy streak at both positive and negative κ values (Figures 7b and 7c). Again, these streaks were amplified relative to the shore, and their $\kappa-f$ combinations agree with theoretical bar-trapped modes (Figures 7e and 7f). However, compared to the mild wave condition, energies were more spread in $\kappa-f$ space (especially for the severe condition).

For all wave conditions of the first storm event, surface elevation spectra computed at the inner bar showed no sign of significant (bar-trapped) edge waves (not shown). This indicates that the motions near the inner bar and near the shoreline were dominated by leaky waves. Results of the second storm event were qualitatively similar to the results of the first storm event. For all three conditions of the second storm event, edge waves were observed at the outer bar, whereas edge waves were not observed at the inner bar and near the shoreline.

To quantify the contributions of the edge-wave and the leaky-wave motions, Figure 8 shows the cross-shore variation of the relative contribution (in %) of the edge-wave band and the leaky-wave band to the total energy of the surface elevation spectra at the infragravity frequencies (which add up to approximately 100%). For all conditions, relative contributions of the leaky and edge-wave band were roughly constant throughout the domain, except near the outer bar where the contribution of the edge-wave band generally increased significantly (except for the severe condition of the first storm event). This local increase in the edge-wave contribution was most significant for the moderate wave conditions (especially for the first storm event), whereas it was smaller for the more energetic wave conditions. For increasingly energetic conditions, the overall contribution of the edge-wave band decreased, and the contribution of the leaky-wave band increased. This is likely related to the mean-wave angle, which decreased for increasingly energetic conditions (Table 1). Although the partitioning of the wave number spectra did not distinguish between bound and free waves, these results suggest that leaky waves dominated over edge waves throughout most of the nearshore, except near the outer bar.

The local increase of the edge-wave contribution at the outer bar coincides with significant contributions of bar-trapped edge waves. Bar-trapped motions were only energetic near the outer bar, and decreased significantly away from the bar. Their relative contribution was largest for the mild wave conditions, and was smaller for more energetic conditions (especially for the first storm event, Figure 8c). These results suggest that bar-trapped edge waves were responsible for the increased contribution of the edge-wave band near

Table 4. Bar-Trapped Edge-Wave Heights ($H^{bt}_{m_0,ig}$), and (for Reference) Infragravity-Wave Heights ($H_{m_0,ig}$) at the Outer Bar

	E1a	E1b	E1c	E2a	E2b	E2c
$H_{m_0,ig}$	0.28	0.39	0.67	0.27	0.34	0.57
$H^{bt}_{m_0,ig}$	0.19	0.18	0.19	0.15	0.18	0.23

the outer bar, and (partially) explain the local maximum of $H_{m_0,ig}$ near the outer bar (as previously observed in section 3, Figures 3f–3h). Although the relative contribution of bar-trapped edge waves reduced for both events, the bar-trapped wave height ($H^{bt}_{m_0,ig}$) remained approximately constant for increasingly energetic conditions of the first storm event, and gradually increased during the second storm event (Table 4).

4.2. Infragravity Energy Balance: Flux Gradients, Nonlinear Energy Transfers, and Dissipation

To gain insight in the infragravity energy balance throughout the nearshore, Figures 9a–9f show the cross-shore variation of the frequency integrated energy flux gradients $\partial F\left(=\partial F_x/\partial x+\partial F_y/\partial y\right)$, nonlinear energy transfer term W, and the dissipation due to bottom friction D_b. For all conditions, $\partial F_y/\partial y$ was typically small compared to ∂F, indicating that $\partial F_x/\partial x$ dominated ∂F.

For both mild conditions, the significant flux gain near the outer bar was partially balanced by the nonlinear transfer term W (Figures 9a and 9d). Further shoreward, the positive ∂F just seaward of the inner bar was

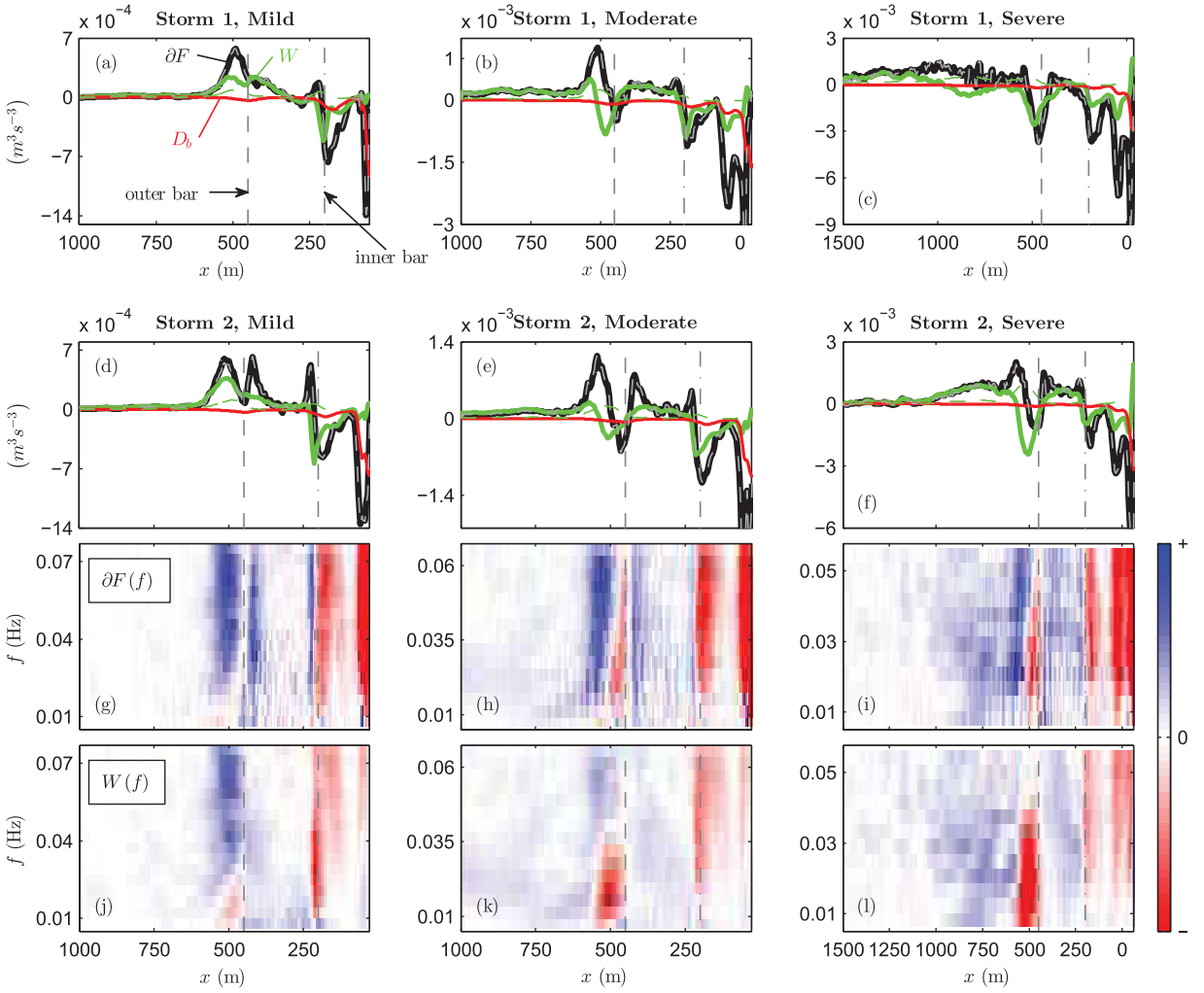

Figure 9. (a–f) Cross-shore variation of the frequency integrated energy flux gradient $\partial F\left(=\partial F_x/\partial x+\partial F_y/\partial y\right)$ (black line); nonlinear transfer term W (green line); and bulk dissipation by bottom friction D_b (red line); for the (left) mild, (middle) moderate, and (right) severe condition of the (a–c) first and (d–f) second storm event. (g–l) The corresponding cross-shore variation of $\partial F(f)$, and $W(f)$ for the second storm event. All frequency-dependent terms in Figures 9g–9l are normalized by the maximum value of $\partial F(f)$; therefore, colors indicate the relative magnitude of these terms. In Figures 9a–9f, the thin gray dashed lines represent $\partial F_x/\partial x$ and the dashed green line represents the S_{yy} contribution to W. In all plots, the thin vertical lines indicate the approximate location of the outer (dashed line) and inner bar (dash dotted line).

not balanced by W, whereas W did explain part of the negative ∂F just shoreward of this location. Near the shoreline ($x < 150$ m), the flux decreased significantly, which was not explained by W. However, the bottom dissipation term D_b did partially balance the negative ∂F near the shoreline. Qualitatively similar patterns were observed for the moderate conditions (Figures 9a and 9e), and the severe condition of the second storm. The main difference between the more energetic and mild conditions occurred near the outer bar, where ∂F was locally negative, which was partially reflected in W. For the severe condition of the first storm, the flux increase seaward of the outer bar was more gradual and spread over the cross shore, which was only partially explained by W (Figure 9c). For all conditions, the S_{xy} contributions to W were insignificant. The S_{yy} contributions were only significant seaward of the inner bar, at locations where waves were breaking. This dominance of the S_{xx} contribution to the W term is similar to the findings of a previous numerical study at a gently sloping, single barred beach [*Van Dongeren et al*., 2003].

Next, we study how flux gradients and nonlinear transfer terms vary with frequency over the nearshore. Here we focus on the results of the second storm event (Figures 9g–9i), which where qualitatively representative for the first storm. Overall, the frequency-dependent flux gradient $\partial F(f)$ mirrored the bulk term ∂F as patterns were relatively spread over the frequencies. However, variations in frequency were observed near the outer and inner bar. Near the outer bar, for all three conditions, flux gains were concentrated at higher frequencies, whereas flux losses were larger at lower frequencies (e.g., Figure 9h). Near the inner bar, both flux gains and losses were typically concentrated at higher frequencies (e.g., Figure 9g). At first sight, patterns of $W(f)$ appear to be qualitatively similar to $\partial F(f)$ patterns. However, similar to the bulk terms, $W(f)$ did not fully balance significant flux gains near the outer bar, and did not explain the energy gains near the inner bar and the energy losses near the shoreline. Furthermore, $W(f)$ estimates suggest greater flux losses than $\partial F(f)$ near the outer bar.

Close to the shoreline ($x \leq 150$ m), strong negative flux gradients occurred, whereas the nonlinear transfer term was near zero. The bottom friction term only balanced part of these significant flux losses, which suggests that another process contributed to these flux losses. These significant flux losses were supported by the low R^2 values, which also indicated significant nearshore energy losses (Table 3). However, the bulk reflection coefficients and the nearshore energy balance did not discriminate between the effect of wave trapping and actual dissipation. To study if topographic trapping affected the nearshore energy balance, Figures 10a–10c show the shoreward and seaward directed x-component of the linear energy flux, in $\kappa - f$ space, near the shoreline ($d \approx 1$ m), for the three conditions of the first storm event. This analysis excluded the nonlinear flux contribution, which was small near the shoreline (Figure 6). For all three conditions, regions of significant seaward fluxes mirrored regions of significant shoreward fluxes. The seaward fluxes were smaller than the shoreward fluxes over the whole range of $\kappa - f$ combinations. Shoreward and seaward fluxes showed no sign of significant edge-wave motions, which confirms that the wave motion near the shoreline was dominated by leaky waves. This suggests that the small seaward fluxes were due to significant dissipation of shoreward-propagating energy, rather than due to trapping shoreward of $d \approx 1$ m. Similar results were observed for the three cases of the second storm event (not shown). This leaves infragravity-wave breaking as possible dissipation mechanism that contributed to the significant infragravity energy losses. The magnitude of the predicted R^2 and its frequency dependence is similar to the findings of *de Bakker et al*. [2014], who conducted an observational study at the same field site. They linked these small shoreline reflections to the occurrence of infragravity-wave breaking, which they hypothesized to be the dominant dissipation mechanism. The consistency between this study and the results of *de Bakker et al*. [2014], and our observations that bottom friction only partially balanced the negative flux gradients near the shoreline, indicates that infragravity-wave breaking likely contributed to the energy flux losses at the higher infragravity frequencies.

To study if the nearshore dissipation varied in alongshore direction, Figures 10d–10f show the alongshore variation of the bulk-infragravity reflection coefficient $R^2(y)$ for the conditions of the first storm event. $R^2(y)$ varied with a maximal factor of two along the coast. Largest reflections typically occurred near relative steep normalized bed slopes β_h, and alongshore variations of R^2 mirrored variations in β_h. These results of the first storm event are representative for the results of the second storm event. The typical qualitative agreement between R^2 and β_h patterns illustrates the strong relation between the infragravity reflections and the normalized bed slope [e.g., *van Dongeren et al*., 2007; *de Bakker et al*., 2014].

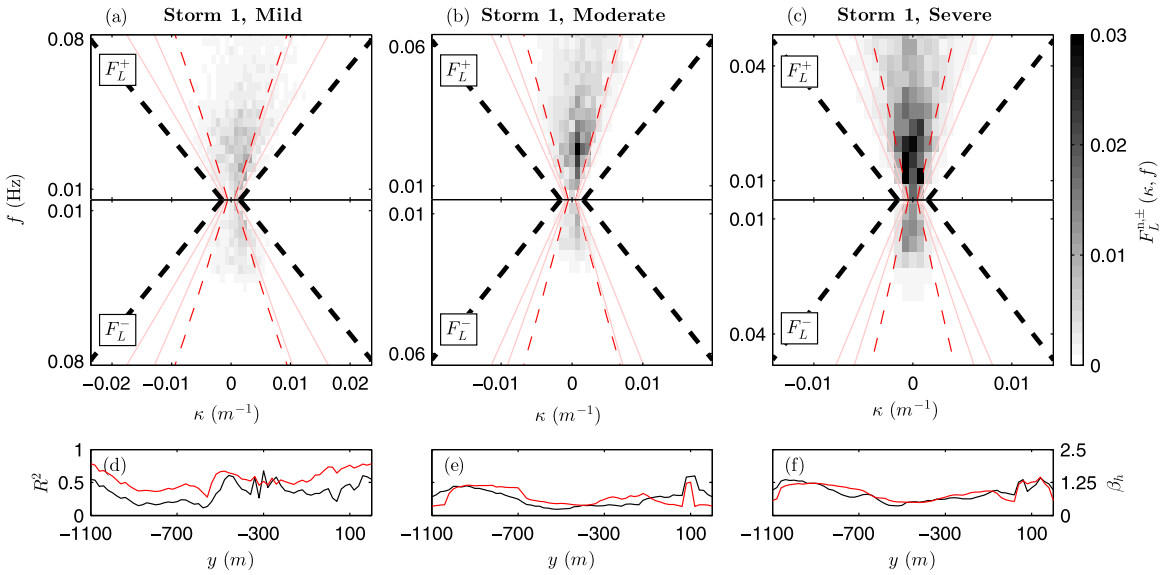

Figure 10. (a–c) Incoming and outgoing cross-shore linear energy flux $F_L^{\pm}(\kappa, f)$ at $d \approx 1$ m, normalized by the total incoming linear energy flux, for the (a) mild, (b) moderate, and (c) severe wave condition of the first storm event. The thick dashed line indicates the shallow-water phase velocity, which is the lower limit of validity of the WKB approximation. The dashed red lines indicate the leaky-wave cutoff, and the light red lines bound the theoretical region of edge waves that are trapped at the outer bar ($c = \sqrt{g d^*_{\text{bar}}}$, and $c = \sqrt{g d^*_{\text{trough}}}$, where d^*_{bar} and d^*_{trough} indicate the effective depth at the outer bar and in the trough, respectively). (d–f) Alongshore variation of the bulk reflection coefficient R^2 at the approximate location of the 0.5 m depth contour (black line, left axis) and the normalized bed slope β_h (red line, right axis), for the (d) mild, (e) moderate, and (f) severe condition of the first storm event. The normalized bed slope is defined as $\beta_h \left(= \frac{\beta T}{2\pi} \sqrt{\frac{g}{H^+}} \right)$ [*van Dongeren et al.*, 2007], where H^+ is the height of an incoming infragravity wave, T is its period, and β is the bed slope. Here the representative infragravity-wave height and period were computed from the incoming linear energy flux ($H^+ = 4\sqrt{m_0^+}$, and $T = \left(\frac{m_1^+}{m_0^+}\right)^{-1}$, where m_0^+ and m_1^+ are the zeroth and first-order moment of the incoming linear energy flux), and the bed slope was taken as the slope between the mean waterline and 0.5 m depth.

5. Discussion

This study highlighted that, seaward of the inner bar, nonlinear interactions between short and infragravity waves caused an infragravity energy growth. This growth is consistent with the findings of *Henderson et al.* [2006] near a bar at a gently sloping sandy beach. The nonlinear transfers reduced when waves were breaking, and even caused losses at lower infragravity frequencies. This negative work by short waves was stronger and spread to higher frequencies for more intense breaking conditions. Near the inner bar, where short waves were always breaking for the conditions considered in this study, short waves caused negative work at most infragravity frequencies. Similar losses under breaking conditions were previously found based on numerical modeling at a plane beach [*Ruju et al.*, 2012]; and based on field observations at a dissipative beach [*Guedes et al.*, 2013], and near the crest of a coral reef [*Péquignet et al.*, 2014].

Near the shoreline, the significant infragravity energy losses were likely due to a combination of bottom friction and infragravity-wave breaking. This adds to the findings of *de Bakker et al.* [2014] at the same field site, who suggested that bottom friction was at best a secondary dissipation mechanism, based on idealized numerical modeling of a low-sloping (1:80) plane beach for which infragravity reflections were small. For more reflective conditions, the numerical study of *Rijnsdorp et al.* [2014] showed that variations in the bottom friction coefficient significantly affected the nearshore dissipation of infragravity waves. This suggests that the effect of bottom friction is more important for reflective conditions, in line with the findings of this study.

Previous field studies at a barred beach, located near Duck (North Carolina, USA), found that bar-trapped edge waves existed at both infragravity and short-wave frequencies [*Bryan and Bowen*, 1996; *Bryan et al.*, 1998; *Bryan and Bowen*, 1998]. *Bryan et al.* [1998] further found that the bar-trapped waves were energetic for a range of wave conditions. Although these studies qualitatively showed that bar-trapped waves can be energetic, they did not quantify the contributions of the bar-trapped waves. *Van Dongeren et al.* [2003] did quantify the bar-trapped contributions at this field site, based on numerical predictions of the local infragravity-wave field. However, they only considered one wave condition, for which they found that bar-trapped edge waves accounted for 12% of the infragravity energy at the location of the bar. Compared to the Duck field site, the bar system at the Egmond field site was more pronounced (in terms of trough width,

bar width, and bar height). A pronounced bar system is a favorable condition for bar trapping [e.g., *Bryan and Bowen*, 1996]. Indeed, we found that bar-trapped edge waves were energetic at the outer bar, where their contribution to the total infragravity energy ranged 10–50%.

6. Conclusions

This paper has presented the results of a comprehensive numerical study into the infragravity-wave dynamics at a gently sloping, barred beach. To study the temporal and spatial variability of the infragravity-wave dynamics, the nonhydrostatic wave-flow model SWASH has been used to simulate three wave conditions (ranging from relatively mild to severe conditions) of two consecutive storm events. We found that the model produced a wavefield that is representative of the natural conditions, given the reasonable model-data agreement for bulk and frequency-dependent wave parameters (see Figures 3–5 and Table 2). This supports the model application to analyze the infragravity-wave dynamics in more detail.

For all conditions, the infragravity-wave field was dominated by leaky-wave motions throughout the nearshore, except near the outer bar. Here bar-trapped edge waves were generally observed at the infragravity frequencies. The relative contribution of bar-trapped waves was most significant for the mild wave conditions, during which they explained up to 50% of the infragravity energy at the outer bar. For more energetic conditions, their relative contribution reduced, although it remained significant (ranging 10%–40%). In contrast, their absolute contribution remained relatively constant during the first storm event, and gradually increased during the second storm event.

The significant growth of infragravity energy flux near the outer bar (especially for milder conditions) was partly explained by nonlinear energy transfers from short waves. For increasingly energetic conditions, when short-wave breaking intensified at the outer bar, the nonlinear transfers reduced significantly and changed sign at lower infragravity frequencies, causing energy losses at these frequencies. Shoreward of the inner bar, infragravity waves primarily lost energy, which was due to a combination of nonlinear transfers, bottom friction, and infragravity-wave breaking. Nonlinear transfers caused some energy losses near the inner bar, where waves were breaking for all conditions. The strongest infragravity losses occurred near the shoreline, where nonlinear transfers ceased. These significant losses were likely caused by the combined effect of bottom friction and infragravity-wave breaking.

This study has exemplified the application of the SWASH model to study wave dynamics at field scales. The successful application of the model to analyze the infragravity-wave dynamics has illustrated that the model can be a valuable tool to improve our understanding of complex nearshore wave dynamics, at scales not easily covered by in situ observations.

Appendix A: Numerical Wavemaker

At the numerical wavemaker, the horizontal velocities normal to the boundary were prescribed based on a target variance density spectrum $E(f)$. The spectrum was sampled with N discrete frequencies from $f_p/2 < f \leq 3f_p$ with intervals of Δf. To avoid repetition of the wave signal, the frequency interval was set at $\Delta f = 1/T_s$, where T_s is the duration of the simulation (excluding spin-up). Each frequency corresponds to a free long-crested wave with frequency f_n, wave number k_n, amplitude $a_n\left(=\sqrt{2\Delta f E_n}\right)$, random phase ϕ_n, and direction θ_n. For each frequency, the wave direction was randomly drawn using a $\cos^m\theta$ distribution as a probability density function, which was centered at a mean-wave angle $\bar{\theta}(f)$ that varied over the frequencies. At each frequency, the power m was computed from the directional spreading $\sigma_\theta(f)$. To ensure that waves are periodic in alongshore direction, θ_n was adjusted such that the alongshore wave number is an integer multiple of $2\pi/L_y$ [e.g., *Van Dongeren et al.*, 2003], where L_y is the length of the domain in y direction. This approach prevents the standing wave issues of *Johnson and Pattiaratchi* [2006], because the resulting wavefield is homogeneous [*Miles and Funke*, 1989], but requires a large number of wave components to generate a realistic directional wavefield.

The (target) horizontal velocity signal u_t, including a second-order correction to account for incident bound infragravity waves (based on weakly nonlinear wave theory), is given by

$$u_t(x,y,z,t)=\sum_{n=1}^{N}\hat{u}_n(z)\cos\left(2\pi f_n t+\phi_n+k_n(\cos(\theta_n)x+\sin(\theta_n)y)\right)$$
$$+\sum_{n=1}^{N}\sum_{m=n+1}^{N}\hat{u}_{nm}(z)\cos\left(2\pi f_{nm} t+\phi_{nm}+k_{nm}(\cos(\theta_{nm})x+\sin(\theta_{nm})y)\right), \quad \text{(A1)}$$

where N is the number of free wave components. The first term on the right-hand side represents the linear free wave contributions, where $\hat{u}_n(z)$ is the vertically varying velocity amplitude of the nth wave component, which is related to the wave amplitude (a_n) by linear wave theory [e.g., *Holthuijsen*, 2007]. The second term on the right-hand side of (A1) represents the bound infragravity-wave components, where $f_{nm}(=f_m-f_n)$ is the frequency, $\phi_{nm}=(\phi_n-\phi_m+\pi)$ is the phase, k_{nm} is the wave number, θ_{nm} is the direction, and $\hat{u}_{nm}(z)$ is the vertically varying velocity amplitude of a bound infragravity-wave component forced by the difference interaction between the nth and mth free wave component. The bound wave number is defined as

$$k_{nm}=\sqrt{k_n^2+k_m^2+2k_nk_m\cos(\theta_n-\theta_m+\pi)}, \quad \text{(A2)}$$

and the bound wave angle as

$$\theta_{nm}=\arctan\left(\frac{k_m\sin\theta_m-k_n\sin\theta_n}{k_m\cos\theta_m-k_n\cos\theta_n}\right). \quad \text{(A3)}$$

In coastal waters, infragravity waves are essentially shallow-water waves for which the vertical variation of $\hat{u}_{nm}$ is negligible. Therefore, $\hat{u}_{nm}(z)$ is approximated with a vertically constant velocity amplitude, which is computed based on the free wave components following *Hasselmann* [1962], see Appendix B.

To absorb outgoing waves and to prevent rereflections at the wave maker, the total velocity signal was defined as a superposition of the target (or incident) velocity signal and the velocity signal of reflected waves (u_r), $u=u_t+u_r$. To estimate u_r, outgoing waves were assumed to be shallow-water waves propagating perpendicular to the boundary. In this manner, u_r was computed as, following mass conservation in combination with the assumption that outgoing waves are progressive and of constant form,

$$u_r=\frac{c}{d}\zeta_r, \quad \text{(A4)}$$

where $c\left(=\sqrt{gd}\right)$ is the phase velocity of a shallow-water wave, and ζ_r is surface elevation of the outgoing waves, which was detected as the difference between the target surface elevation and the instantaneous surface elevation computed by SWASH.

In this wavemaker implementation, velocities are directly imposed at the offshore boundary, in contrast with the approach typically used in Boussinesq models, which combines a source function to generate waves, and a sponge layer to absorb outgoing waves [e.g., *Wei et al.*, 1999; *Chen et al.*, 2003; *Feddersen et al.*, 2011]. The advantage of the approach used here is that higher-order wave theories can be implemented relatively straightforward to accurately generate nonlinear waves, and a domain extension to accommodate the sponge layer and source region is not required (reducing computational costs). On the other hand, the approach to absorb outgoing waves (A4) is primarily effective for (nearly) shore normal propagating shallow-water waves, whereas it is (weakly) reflective for directional, dispersive waves. In contrast, the sponge layer approach is very effective to damp outgoing waves. However, at low sloping beaches studied in this paper, the reflection of short-waves is typically small. Furthermore, the predicted infragravity reflections were typically small (see sections 3 and 4). Although the wavemaker possibly reflected some outgoing wave energy, we did not notice adverse effects of rereflections at the wavemaker.

Appendix B: Second-Order Boundary Condition

The second-order boundary condition implemented in SWASH is based on weakly nonlinear second-order finite-depth wave theory [*Hasselmann*, 1962]. Herein, the wave field is composed of first-order waves, the free wave response, and a second-order correction, which represents the bound sub and super harmonics. In this study, super harmonics are excluded and the second-order correction only accounts for the sub harmonics (i.e., bound infragravity waves). The amplitude of a bound infragravity wave, forced by two free wave components with frequency f_n and f_m, is given by [*Hasselmann*, 1962]

$$a_{nm}=D_{nm}a_n a_m, \tag{B1}$$

where a_n and a_m are the amplitudes of the respective free wave components and D_{nm} is the interaction coefficient. For directionally spread waves, the interaction coefficient is given by

$$D_{nm}=\frac{gk_nk_m}{2\omega_n\omega_m}\cos(\theta_n-\theta_m+\pi)+\frac{\omega_n^2-\omega_n\omega_m+\omega_m^2}{2g}-C\frac{g(\omega_n-\omega_m)}{\omega_n\omega_m\left[gk_{nm}\tanh(k_{nm}d)-(\omega_n-\omega_m)^2\right]}, \tag{B2}$$

where $\omega(=2\pi f)$ is the radial frequency, and coefficient C is defined as

$$C=(\omega_n-\omega_m)\left(\frac{(\omega_n\omega_m)^2}{g^2}-k_nk_m\cos(\theta_n-\theta_m+\pi)\right)-\frac{1}{2}\left(\frac{\omega_nk_m^2}{\cosh^2(k_md)}-\frac{\omega_mk_n^2}{\cosh^2(k_nd)}\right). \tag{B3}$$

The vertically constant velocity amplitude $\hat{u}_{nm}$ follows from mass conservation in combination with the assumption that bound infragravity waves are progressive and of constant form, $\hat{u}_{nm}=a_{nm}c_g/d$, where c_g $(=2\pi f_{nm}/k_{nm})$ is the group velocity.

Appendix C: Target Wave Conditions

The target wave conditions at the numerical wave maker ($E(f)$, $\bar{\theta}(f)$, and $\sigma_\theta(f)$) were computed using SWAN (version 40.91A), including all deep and shallow wave physics (in default settings). The western boundary in SWAN was taken as a straight line from south to north through the buoy (see Figure 2). At this boundary, the incident wave conditions were considered to be uniform and were given by a JONSWAP shape spectrum, based on the deep water wave parameters ($H_{m_0,d}$, $T_{p,d}$ and $\bar{\theta}_d$), with a $\cos^m\theta$ directional distribution. Unfortunately, no measurements of the directional spreading were available, therefore, we assumed $\sigma_{\theta,d}=30^o$ for all frequencies. No wave information was available at the northern and southern SWAN boundaries, therefore, no incident waves were forced at these boundaries. Although this introduced errors in the region near these boundaries, these local errors did not affect the predicted target wave conditions, because the lateral boundaries were located sufficiently far away from the region of interest. A spatially constant wind field was forced based on the wind measurements at gauge 7a. The frequency range in the SWAN simulations was $0.6f_p-3f_p$ with a resolution of $\Delta f\approx 0.1f$ and the spectral range was $0-360^o$ with a resolution of $\Delta\theta=10^o$. The SWAN predicted target wave conditions ($E(f)$, $\theta(f)$, and $\sigma_\theta(f)$) were output in the center of the SWASH wavemaker (see Figure 2), see Table 1 for an overview of the target bulk wave parameters.

Acknowledgments

Dirk Rijnsdorp thanks Pieter Smit and Julie Pietrzak for their insights and fruitful discussions. The authors thank Falk Feddersen and two anonymous reviewers for their feedback which helped to improve the manuscript significantly. The numerical model output, used to construct results in this work, is available and can be obtained by contacting Dirk Rijnsdorp (D.P.Rijnsdorp@tudelft.nl). Similarly, the field measurement data are available and can be obtained by contacting Gerben Ruessink (B.G.Ruessink@uu.nl). This work is part of the research program Cooperation China (NSFC), which is (partly) financed by the Netherlands Organisation for Scientific Research (NWO). Furthermore, this work was financially supported by NWO "Exacte Wetenschappen" for the use of supercomputer facilities. Finally, Gerben Ruessink acknowledges funding by NWO under contract 821.01.012.

References

Ai, C., and S. Jin (2012), A multi-layer non-hydrostatic model for wave breaking and run-up, *Coastal Eng.*, *62*, 1–8, doi:10.1016/j.coastaleng.2011.12.012.

Bai, Y., and K. F. Cheung (2012), Depth-integrated free-surface flow with a two-layer non-hydrostatic formulation, *Int. J. Numer. Methods Fluids*, *69*(2), 411–429, doi:10.1002/fld.2566.

Bai, Y., and K. F. Cheung (2013), Depth-integrated free-surface flow with parameterized non-hydrostatic pressure, *Int. J. Numer. Methods Fluids*, *71*(2), 403–421, doi:10.1002/fld.3664.

Booij, N., R. C. Ris, and L. H. Holthuijsen (1999), A third-generation wave model for coastal regions: 1. Model description and validation, *J. Geophys. Res.*, *104*(C4), 7649–7666, doi:10.1029/98JC02622.

Bowers, E. C. (1977), Harbour resonance due to set-down beneath wave groups, *J. Fluid Mech.*, *79*(1), 71–92, doi:10.1017/S0022112077000044.

Bryan, K. R., and A. J. Bowen (1996), Edge wave trapping and amplification on barred beaches, *J. Geophys. Res.*, *101*(C3), 6543–6552, doi:10.1029/95JC03627.

Bryan, K. R., and A. J. Bowen (1998), Bar-trapped edge waves and longshore currents, *J. Geophys. Res.*, *103*(C12), 27,867–27,884, doi:10.1029/98JC02098.

Bryan, K. R., P. A. Howd, and A. J. Bowen (1998), Field observations of bar-trapped edge waves, *J. Geophys. Res.*, *103*(C1), 1285–1305, doi:10.1029/97JC02938.

Casulli, V., and G. Stelling (1998), Numerical simulation of 3D quasi-hydrostatic, free-surface flows, *J. Hydraul. Eng.*, *124*(7), 678–686.

Chen, Q., J. T. Kirby, R. A. Dalrymple, F. Shi, and E. Thornton (2003), Boussinesq modeling of longshore currents, *J. Geophys. Res.*, *108*(C11), 3362, doi:10.1029/2002JC001308.

Clark, D. B., S. Elgar, and B. Raubenheimer (2012), Vorticity generation by short-crested wave breaking, *Geophys. Res. Lett.*, *39*, L24604, doi:10.1029/2012GL054034.

Cui, H., J. Pietrzak, and G. Stelling (2012), Improved efficiency of a non-hydrostatic, unstructured grid, finite volume model, *Ocean Modell.*, *54–55*, 55–67, doi:10.1016/j.ocemod.2012.07.001.

Cui, H., J. Pietrzak, and G. Stelling (2014), Optimal dispersion with minimized Poisson equations for non-hydrostatic free surface flows, *Ocean Modell.*, *81*, 1–12, doi:10.1016/j.ocemod.2014.06.004.

de Bakker, A. T. M., M. F. S. Tissier, and B. G. Ruessink (2014), Shoreline dissipation of infragravity waves, *Cont. Shelf Res.*, *72*, 73–82, doi:10.1016/j.csr.2013.11.013.

de Bakker, A. T. M., T. H. C. Herbers, P. B. Smit, M. F. S. Tissier, and B. G. Ruessink (2015), Nonlinear infragravity wave interactions on a gently sloping laboratory beach, *J. Phys. Oceanogr.*, *45*, 589–605, doi:10.1175/JPO-D-14-0186.1.

Feddersen, F. (2013), The generation of surfzone eddies in a strong alongshore current, *J. Phys. Oceanogr.*, *44*(2), 600–617, doi:10.1175/JPO-D-13-051.1.

Feddersen, F., R. T. Guza, S. Elgar, and T. H. C. Herbers (1998), Alongshore momentum balances in the nearshore, *J. Geophys. Res.*, *103*(C8), 15,667–15,676, doi:10.1029/98JC01270.

Feddersen, F., E. L. Gallagher, R. T. Guza, and S. Elgar (2003), The drag coefficient, bottom roughness, and wave-breaking in the nearshore, *Coastal Eng.*, *48*(3), 189–195, doi:10.1016/S0378-3839(03)00026-7.

Feddersen, F., D. B. Clark, and R. T. Guza (2011), Modeling surf zone tracer plumes: 1. Waves, mean currents, and low-frequency eddies, *J. Geophys. Res.*, *116*, C11027, doi:10.1029/2011JC007210.

Guedes, R. M. C., K. R. Bryan, and G. Coco (2013), Observations of wave energy fluxes and swash motions on a low-sloping, dissipative beach, *J. Geophys. Res. Oceans*, *118*, 3651–3669, doi:10.1002/jgrc.20267.

Guza, R., and E. Thornton (1982), Swash oscillations on a natural beach, *J. Geophys. Res.*, *87*(1), 483–491, doi:10.1029/JC087iC01p00483.

Guza, R. T., and E. B. Thornton (1985), Observations of surf beat, *J. Geophys. Res.*, *90*(C2), 3161–3172, doi:10.1029/JC090iC02p03161.

Hasselmann, K. (1962), On the non-linear energy transfer in a gravity-wave spectrum. Part 1. General theory, *J. Fluid Mech.*, *12*(4), 481–500, doi:10.1017/S0022112062000373.

Henderson, S. M., and A. Bowen (2002), Observations of surf beat forcing and dissipation, *J. Geophys. Res.*, *107*(C11), 3193, doi:10.1029/2000JC000498.

Henderson, S. M., R. T. Guza, S. Elgar, T. H. C. Herbers, and A. J. Bowen (2006), Nonlinear generation and loss of infragravity wave energy, *J. Geophys. Res.*, *111*, C12007, doi:10.1029/2006JC003539.

Herbers, T. H. C., S. Elgar, and R. T. Guza (1995), Generation and propagation of infragravity waves, *J. Geophys. Res.*, *100*(C12), 24,863–24,872, doi:10.1029/95JC02680.

Holthuijsen, L. H. (2007), *Waves in Oceanic and Coastal Waters*, Cambridge Univ. Press, Cambridge, U. K.

Howd, P. A., J. Oltman-Shay, and R. A. Holman (1991), Wave variance partitioning in the trough of a barred beach, *J. Geophys. Res.*, *96*(C7), 12,781–12,795, doi:10.1029/91JC00434.

Howd, P. A., A. J. Bowen, and R. A. Holman (1992), Edge waves in the presence of strong longshore currents, *J. Geophys. Res.*, *97*(C7), 11,357–11,371, doi:10.1029/92JC00858.

Huntley, D. A., R. T. Guza, and E. B. Thornton (1981), Field observations of surf beat: 1. Progressive edge waves, *J. Geophys. Res.*, *86*(C7), 6451–6466, doi:10.1029/JC086iC07p06451.

Janssen, T. T., J. A. Battjes, and A. R. van Dongeren (2003), Long waves induced by short-wave groups over a sloping bottom, *J. Geophys. Res.*, *108*(C8), 3252, doi:10.1029/2002JC001515.

Johnson, D., and C. Pattiaratchi (2006), Boussinesq modelling of transient rip currents, *Coastal Eng.*, *53*(5–6), 419–439, doi:10.1016/j.coastaleng.2005.11.005.

Kenyon, K. E. (1972), Edge waves with current shear, *J. Geophys. Res.*, *77*(33), 6599–6603, doi:10.1029/JC077i033p06599.

Kirby, J. T., R. A. Dalrymple, and P. L.-F. Liu (1981), Modification of edge waves by barred-beach topography, *Coastal Eng.*, *5*, 35–49, doi:10.1016/0378-3839(81)90003-X.

Kuik, A. J., G. P. van Vledder, and L. H. Holthuijsen (1988), A method for the routine analysis of pitch-and-roll buoy wave data, *J. Phys. Oceanogr.*, *18*(7), 1020–1034, doi:10.1175/1520-0485(1988)018<1020:AMFTRA>2.0.CO;2.

Lippmann, T. C., T. H. C. Herbers, and E. B. Thornton (1999), Gravity and shear wave contributions to nearshore infragravity motions, *J. Phys. Oceanogr.*, *29*, 231–239, doi:10.1175/1520-0485(1999)029<0231:GASWCT>2.0.CO;2.

Longuet-Higgins, M. S., and R. W. Stewart (1960), Changes in the form of short gravity waves on long waves and tidal currents, *J. Fluid Mech.*, *8*(4), 565–583, doi:10.1017/S0022112060000803.

Ma, G., F. Shi, and J. T. Kirby (2012), Shock-capturing non-hydrostatic model for fully dispersive surface wave processes, *Ocean Modell.*, *43–44*, 22–35, doi:10.1016/j.ocemod.2011.12.002.

MacMahan, J. H. (2004), Surf zone eddies coupled with rip current morphology, *J. Geophys. Res.*, *109*, C07004, doi:10.1029/2003JC002083.

Miles, M. D., and E. R. Funke (1989), A comparison of methods for synthesis of directional seas, *J. Offshore Mech. Arct. Eng.*, *111*(1), 43–48, doi:10.1115/1.3257137.

Munk, W. H. (1949), Surf beats, *Trans. AGU*, *30*(6), 849–854, doi:10.1029/TR030i006p00849.

Naciri, M., B. Buchner, T. Bunnik, R. Huijsmans, and J. Andrews (2004), Low frequency motions of LNG carriers moored in shallow water, in *23rd International Conference on Offshore Mechanics and Arctic Engineering*, vol. 3, pp. 995–1006, Am. Soc. of Mech. Eng., doi:10.1115/OMAE2004-51169.

Okihiro, M., R. T. Guza, and R. J. Seymour (1992), Bound Infragravity Waves, *J. Geophys. Res.*, *97*(C7), 11,453–11,469, doi:10.1029/92JC00270.

Oltman-Shay, J., and R. T. Guza (1987), Infragravity edge wave observations on two California beaches, *J. Phys. Oceanogr.*, *17*(5), 644–663, doi:10.1175/1520-0485(1987)017<0644:IEWOOT>2.0.CO;2.

Özkan Haller, H. T., and J. T. Kirby (1999), Nonlinear evolution of shear instabilities of the longshore current: A comparison of observations and computations, *J. Geophys. Res.*, *104*(C11), 25,953–25,984, doi:10.1029/1999JC900104.

Péquignet, A.-C. N., J. M. Becker, and M. A. Merrifield (2014), Energy transfer between wind waves and low-frequency oscillations on a fringing reef, Ipan Guam, *J. Geophys. Res. Oceans*, *119*, 6709–6724, doi:10.1002/2014JC010179.

Pomeroy, A., R. Lowe, G. Symonds, A. Van Dongeren, and C. Moore (2012), The dynamics of infragravity wave transformation over a fringing reef, *J. Geophys. Res.*, *117*, C11022, doi:10.1029/2012JC008310.

Reniers, A. J. H. M., J. H. MacMahan, E. B. Thornton, and T. P. Stanton (2007), Modeling of very low frequency motions during RIPEX, *J. Geophys. Res.*, *112*, C07013, doi:10.1029/2005JC003122.

Rijnsdorp, D. P., P. B. Smit, and M. Zijlema (2014), Non-hydrostatic modelling of infragravity waves under laboratory conditions, *Coastal Eng.*, *85*, 30–42, doi:10.1016/j.coastaleng.2013.11.011.

Ruessink, B. G. (2010), Observations of turbulence within a natural surf zone, *J. Phys. Oceanogr.*, *40*(12), 2696–2712, doi:10.1175/2010JPO4466.1.

Ruessink, B. G., I. M. J. van Enckevort, K. S. Kingston, and M. A. Davidson (2000), Analysis of observed two- and three-dimensional nearshore bar behaviour, *Mar. Geol.*, *169*(1–2), 161–183, doi:10.1016/S0025-3227(00)00060-8.

Ruessink, B. G., J. R. Miles, F. Feddersen, R. T. Guza, and S. Elgar (2001), Modeling the alongshore current on barred beaches, *J. Geophys. Res.*, *106*(C10), 22,451–22,463, doi:10.1029/2000JC000766.

Ruju, A., J. L. Lara, and I. J. Losada (2012), Radiation stress and low-frequency energy balance within the surf zone: A numerical approach, *Coastal Eng.*, *68*, 44–55, doi:10.1016/j.coastaleng.2012.05.003.

Ruju, A., J. L. Lara, and I. J. Losada (2014), Numerical analysis of run-up oscillations under dissipative conditions, *Coastal Eng.*, *86*, 45–56, doi: 10.1016/j.coastaleng.2014.01.010.
Russell, P. E. (1993), Mechanisms for beach erosion during storms, *Cont. Shelf Res.*, *13*(11), 1243–1265, doi:10.1016/0278-4343(93)90051-X.
Schönfeldt, H.-J. (1994), Randwellen in der Ostsee und anomale Dispersion in der Brandungszone, *Dtsch. Hydrogr. Z.*, *46*(1), 81–98, doi: 10.1007/BF02225742.
Sheremet, A., R. T. Guza, S. Elgar, and T. H. C. Herbers (2002), Observations of nearshore infragravity waves: Seaward and shoreward propagating components, *J. Geophys. Res.*, *107*(C8), 3095, doi:10.1029/2001JC000970.
Sheremet, A., R. T. Guza, and T. H. C. Herbers (2005), A new estimator for directional properties of nearshore waves, *J. Geophys. Res.*, *110*, C01001, doi:10.1029/2003JC002236.
Smit, P., M. Zijlema, and G. Stelling (2013), Depth-induced wave breaking in a non-hydrostatic, near-shore wave model, *Coastal Eng.*, *76*, 1–16, doi:10.1016/j.coastaleng.2013.01.008.
Smit, P., T. Janssen, L. Holthuijsen, and J. Smith (2014), Non-hydrostatic modeling of surf zone wave dynamics, *Coastal Eng.*, *83*, 36–48, doi: 10.1016/j.coastaleng.2013.09.005.
Stelling, G., and M. Zijlema (2003), An accurate and efficient finite difference algorithm for non hydrostatic free surface flow with application to wave propagation, *Int. J. Numer. Methods Fluids*, *43*, 1–23, doi:10.1002/fld.595.
Stelling, G. S., and S. P. A. Duinmeijer (2003), A staggered conservative scheme for every Froude number in rapidly varied shallow water flows, *Int. J. Numer. Methods Fluids*, *43*(12), 1329–1354, doi:10.1002/fld.537.
Symonds, G., D. A. Huntley, and A. J. Bowen (1982), Two-dimensional surf beat: Long wave generation by a time-varying breakpoint, *J. Geophys. Res.*, *87*(C1), 492–498, doi:10.1029/JC087iC01p00492.
Thomson, J., S. Elgar, B. Raubenheimer, T. H. C. Herbers, and R. T. Guza (2006), Tidal modulation of infragravity waves via nonlinear energy losses in the surfzone, *Geophys. Res. Lett.*, *33*, L05601, doi:10.1029/2005GL025514.
Tucker, M. (1950), Surf beats: Sea waves of 1 to 5 min. period, *Proc. R. Soc. London, Ser. A*, *202*(1071), 565–573, doi:10.1098/rspa.1950.0120.
van der Molen, W., P. Monardez, and A. van Dongeren (2006), Numerical simulation of long-period waves and ship motions in Tomakomai Port, Japan, *Coastal Eng. J.*, *48*(1), 59–79, doi:10.1142/S0578563406001301.
Van Dongeren, A., A. Reniers, J. Battjes, and I. Svendsen (2003), Numerical modeling of infragravity wave response during DELILAH, *J. Geophys. Res.*, *108*(C9), 3288, doi:10.1029/2002JC001332.
van Dongeren, A., J. Battjes, T. Janssen, J. van Noorloos, K. Steenhauer, G. Steenbergen, and A. Reniers (2007), Shoaling and shoreline dissipation of low-frequency waves, *J. Geophys. Res.*, *112*, C02011, doi:10.1029/2006JC003701.
Van Dongeren, A., R. Lowe, A. Pomeroy, D. M. Trang, D. Roelvink, G. Symonds, and R. Ranasinghe (2013), Numerical modeling of low-frequency wave dynamics over a fringing coral reef, *Coastal Eng.*, *73*, 178–190, doi:10.1016/j.coastaleng.2012.11.004.
van Thiel de Vries, J. S. M., M. R. A. van Gent, D. J. R. Walstra, and A. J. H. M. Reniers (2008), Analysis of dune erosion processes in large-scale flume experiments, *Coastal Eng.*, *55*(12), 1028–1040, doi:10.1016/j.coastaleng.2008.04.004.
Walters, R. A. (2005), A semi-implicit finite element model for non-hydrostatic (dispersive) surface waves, *Int. J. Numer. Methods Fluids*, *49*(7), 721–737, doi:10.1002/fld.1019.
Webb, S. C., X. Zhang, and W. Crawford (1991), Infragravity waves in the deep ocean, *J. Geophys. Res.*, *96*(C2), 2723–2736, doi:10.1029/90JC02212.
Wei, G., J. T. Kirby, and A. Sinha (1999), Generation of waves in Boussinesq models using a source function method, *Coastal Eng.*, *36*(4), 271–299, doi:10.1016/S0378-3839(99)00009-5.
Wei, Z., and Y. Jia (2014), Non-hydrostatic finite element model for coastal wave processes, *Coastal Eng.*, *92*, 31–47, doi:10.1016/j.coastaleng.2014.07.001.
Yamazaki, Y., Z. Kowalik, and K. F. Cheung (2009), Depth-integrated, non-hydrostatic model for wave breaking and run-up, *Int. J. Numer. Methods Fluids*, *61*(5), 473–497, doi:10.1002/fld.1952.
Yamazaki, Y., K. F. Cheung, and Z. Kowalik (2011), Depth-integrated, non-hydrostatic model with grid nesting for tsunami generation, propagation, and run-up, *Int. J. Numer. Methods Fluids*, *67*(12), 2081–2107, doi:10.1002/fld.2485.
Zijlema, M., and G. S. Stelling (2008), Efficient computation of surf zone waves using the nonlinear shallow water equations with non-hydrostatic pressure, *Coastal Eng.*, *55*(10), 780–790, doi:10.1016/j.coastaleng.2008.02.020.
Zijlema, M., G. Stelling, and P. Smit (2011), SWASH: An operational public domain code for simulating wave fields and rapidly varied flows in coastal waters, *Coastal Eng.*, *58*(10), 992–1012, doi:10.1016/j.coastaleng.2011.05.015.